



Numerical simulation of supersonic condensation flows using Eulerian-Lagrangian and Eulerian wall film models



Hongbing Ding^a, Yu Zhang^a, Chunqian Sun^a, Yan Yang^b, Chuang Wen^{c,*}

^a Tianjin Key Laboratory of Process Measurement and Control, School of Electrical and Information Engineering, Tianjin University, Tianjin, 300072, China

^b Faculty of Engineering, University of Nottingham, Nottingham NG7 2RD, United Kingdom

^c College of Engineering, Mathematics and Physical Sciences, University of Exeter, Exeter EX4 4QF, United Kingdom

ARTICLE INFO

Keywords:

Condensation
Phase change
Droplet formation
Liquid film
Supersonic flow
Performance optimization

ABSTRACT

As a clean and energy-saving natural gas purification and separation device, the supersonic separator's internal gas-liquid separation mechanism needs to be explored. However, the complex three-field (gas, droplet, liquid film) two-phase (gas, liquid) supersonic condensation flow challenges the numerical modeling. Most studies are limited to tracking the gas phase and droplets and ignore the effects of liquid film and phase change on droplets and water vapor removal. In the present study, we established a novel Eulerian-Lagrangian method coupled with the Eulerian wall film model to study the three-field behaviors and phase change for the enhancement of separation efficiency in the supersonic separator. The accuracy of the proposed model was validated by three experiments. The gas, droplet, and liquid film behaviors and three-field heat and mass transfers in the supersonic separator are studied using the proposed three-field two-phase flow model. Then, the sensitivity analysis was carried out, which showed the inlet mass flow rate $q_{p,in}$ of the heterogeneous droplets determines the maximum film thickness. For $q_{p,in} = 0.001 \text{ kg/s}$, this value is about $85.2 \mu\text{m}$. The result also showed a significant improvement in separation efficiency with a proper inlet droplet diameter $d_{p,in}$, $q_{p,in}$, and gas pressure p_{in} . For $d_{p,in}$, $q_{p,in}$, and p_{in} are selected as $2.2 \mu\text{m}$, 0.0015 kg/s , and 3 atm , better separation efficiency can be obtained with droplet removal rate, water vapor removal rate, and dew point depression being optimized to 100%, 57.4%, and 29.1% respectively.

1. Introduction

As a green, safe, affordable, and sustainable energy source, natural gas accounts for a quarter of the world's energy consumption [1–3]. However, in natural gas extraction, a large amount of saturated water vapor can be mixed [4]. Under a high-pressure and low-temperature environment, saturated water vapor or liquid water will form a natural gas hydrate [5], reducing the circulation area of the pipeline and producing throttling [6]. Thus, the pipeline, valves, and other types of equipment will be blocked, seriously affecting the pipeline's safe operation [7]. Therefore, water management is a key issue in natural gas extraction. From the perspective of separation efficiency, the modification of water vapor dew point in natural gas and the natural gas's drying and purification are crucial to maintaining the natural gas transportation pipeline's long-term safe and stable operation [8, 9]. Traditional methods such as absorption, adsorption, cryogenic, and membranes have been used for water management. Nonetheless, their

developments are limited by unfavorable factors such as high cost, complex equipment, and pollution [10, 11]. Supersonic separation technology is a breakthrough in air purification [12], gas dehydration [13, 14], carbon capture [15–17], heavy hydrocarbon removal [18] in the field of petroleum industry [19], chemical industry [20–22] and nuclear industry [23, 24]. It has the advantages of high efficiency [25], low energy consumption, no moving parts [26], low cost, and environmental friendliness, which can provide the same separation efficiency while ensuring economy [27]. Therefore, it is of great significance to fully study the separation process of the supersonic separator, in which accurately predicting condensation and separation performance is a critical task. However, the internal physical mechanism of the supersonic separator is complicated [28] because of the combination of low-temperature condensation and cyclone separation technology [29]. As shown in Fig. 1, it is a difficult supersonic swirling condensation flow process with two phases (gas, liquid) and three fields (gas, droplets, and liquid film) [30]. The three fields have complex mass and heat transfer

* Corresponding author.

E-mail address: c.wen@exeter.ac.uk (C. Wen).

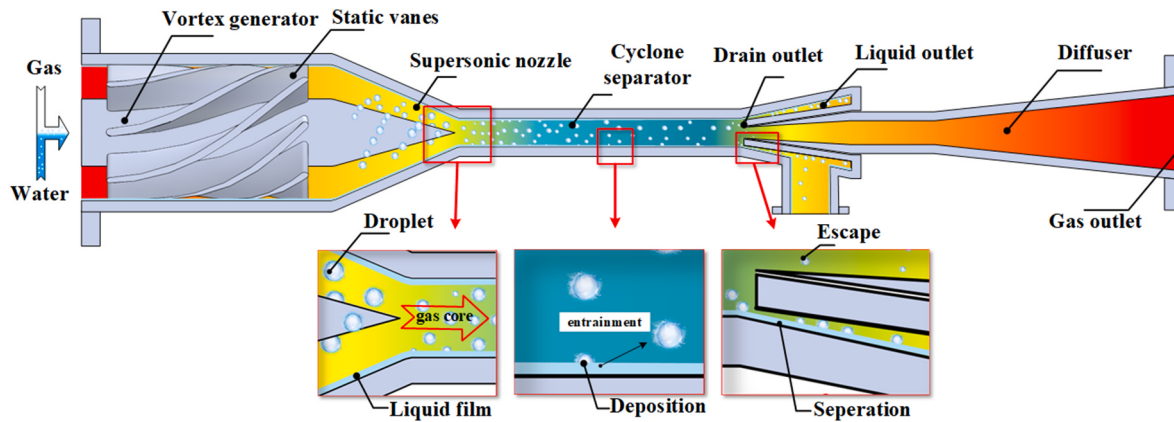


Fig. 1. Typical structure of supersonic separator for gas dehydration and purification.

relationships [31].

As far as we know, the main computational fluid dynamics (CFD) strategies for gas-droplet two-phase separation characteristics of supersonic separators are the Eulerian-Eulerian [32] and Eulerian-Lagrangian [33] methods. Both methods have been proven to have good simulation accuracy for gas-liquid two-phase flow. Further, the Eulerian-Lagrangian approach is superior in capturing the special behavior of droplet collision, motion, and breakage [23]. In previous studies, based on the Eulerian-Lagrangian method, many scholars analyzed the gas-liquid separation process in the supersonic separator and promoted the development of this field. Yang et al. [34] modeled a strong rotating flow supersonic separator to separate particles. The results show that most of the particles were centrifugally separated on the wall or directly to the water outlet due to the strong swirling flow. When the droplet diameter was $1.5 \mu\text{m}$, the separation efficiency of the particle could reach about 80%. Wen et al. [35] made a novel supersonic separator with an annular Laval nozzle. They used a discrete phase model to predict the trajectory of natural airflow and particle separation characteristics in the SS, which increased the separation efficiency of particles to about 94%. Liu et al. [36] established a numerical model by coupling the RSM turbulence model with the discrete phase model and predicted the influence of biological data such as mass flow rate, particle diameter, pressure loss ratio, and cyclone intensity on the droplet separation efficiency of the supersonic separator. Chen et al. [37] used the Eulerian-Lagrangian model to calculate the supersonic separator's flow distribution and droplet trajectory. They found that the cyclone's structure could seriously affect the separation performance of the SS. The prediction method using the discrete phase model was also adopted by Wang et al. [38], which showed that the separation efficiency would increase with the droplet size growth, and the droplet size of $2\text{--}4 \mu\text{m}$ would correspond to the best separation result. These studies have profound significance for the droplet behavior in gas-water separation and prove that the Eulerian-Lagrangian method has unique advantages in simulating droplet behavior and droplet removal rate in the supersonic separator. However, the Eulerian-Lagrangian approach, which has certain limitations, fails to consider the supersonic separator's liquid film formation [39]. For this reason, the Eulerian-Lagrangian approach needs to be coupled with a wall film model [40] to capture a more comprehensive three-field two-phase flow mechanism in the supersonic separator.

A notable feature of the three-field two-phase separation process is that the water vapor's condensation [41] and the deposition of droplets may cause the formation of the liquid film [42]. This phenomenon can be well analyzed by the Eulerian wall film model [43]. Wang et al. [44] combined the Eulerian-Lagrangian model with the Eulerian wall film model to study the separation performance of corrugated plate gas-water separators with different blade types. The optimal geometry was obtained from nine experimental designs based on the selected

parameters. Han et al. [45] used a similar method to study the gas, droplets, and liquid film characteristics in three differently composed baffle separators used for a 75 kW PEMFC system, and a more reasonable baffle separator structure was obtained. Li et al. [46] also used the same way to carry out the numerical calculation on the separation performance of the four designed foggers. The results showed that the separation efficiency of water droplets would change when the droplet diameter changed. The overall separation efficiency of the four types of foggers would gradually stabilize with the increase in inlet flow rate. Yuan et al. [47] used the Eulerian-Lagrangian method to solve the gas-droplet interaction and the Eulerian wall film model to study the emergence and evolution of the liquid film. The results showed that liquid film thickness could have almost no relationship with droplet size and discrete phase content, which mainly affected the separation performance. Deng et al. [48] used the Eulerian-Lagrangian coupled Eulerian wall film model to study the complex process of two-phase three-field flow and successfully obtained the phase exchange in an axial flow cyclone. The results were significant to the design, operation, and optimization of axial flow cyclones. A coupled model of Eulerian wall film model and discrete phase model was applied by Zhou et al. [49] to explore the droplet re-entrainment phenomenon in a baffle demister. The conclusion was drawn that the separation and stripping of the liquid film at the defogger corner would lead to the re-entrainment of droplets. However, although both liquid film and droplet were considered in the above studies, few of them have studied the phase change behaviors such as condensation and evaporation, resulting in a lack of information on the assessment of water vapor removal rate.

Based on the literature review, several scientific gaps are covered in the study of the three-field two-phase condensation flow mechanism of the supersonic separator and the evaluation of its separation efficiency:

- (1) Most numerical studies are generally based on the Eulerian-Lagrangian method, neglecting the liquid film's formation, evaporation, separation, and stripping. The evolution of liquid film in the supersonic separator needs to be explored.
- (2) The detailed description of heat and mass transfer between the gas, droplet, and liquid film in supersonic swirl condensation flow is quite limited. The three-field interactions should be considered for evaluating separation efficiency.
- (3) Considering the three-field coupling, the influence of heterogeneous droplets on flow characteristics, liquid film development, and separation efficiency of supersonic separators is not clear.

The above-mentioned scientific gaps are investigated in this study. The Eulerian-Lagrangian method coupled with the Eulerian wall film model was established for three-field two-phase condensation flow in the supersonic separator. Compared with the above literature, the novelty of this study can be summarized as follows:

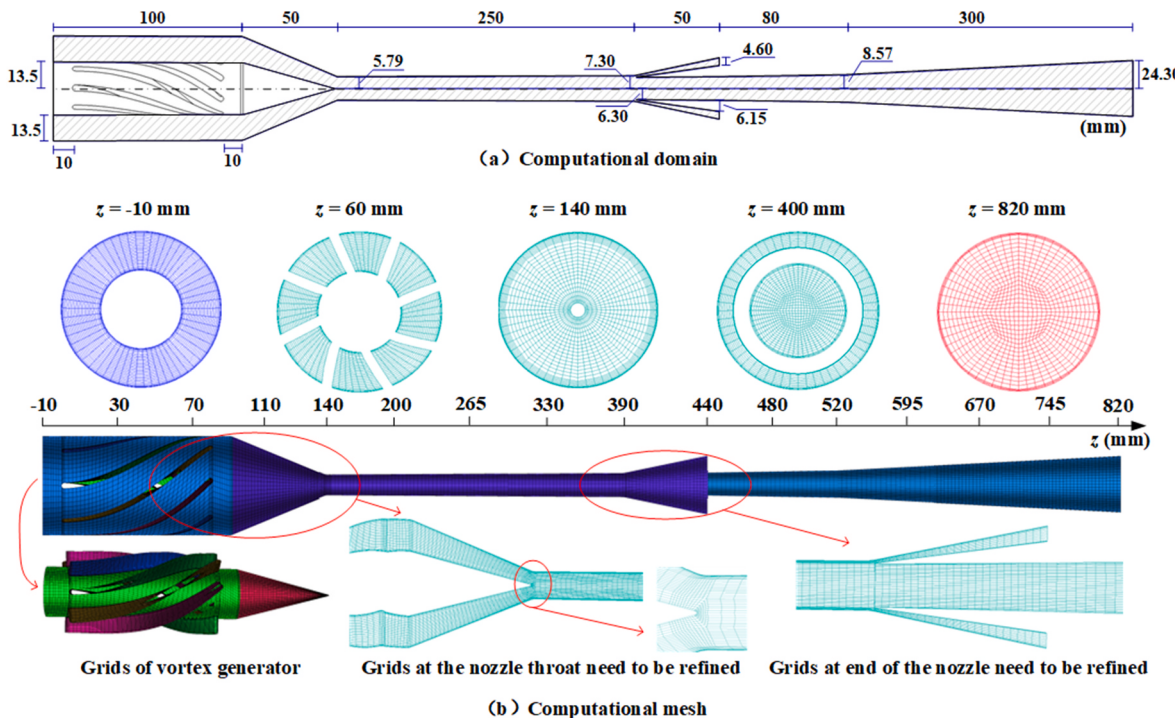


Fig. 2. Computational domain and Computational mesh of the supersonic separator.

- (1) The role of the liquid film in supersonic two-phase flow has not been ignored. On the contrary, it has been well considered in the numerical model. The formation and evolution of liquid film in the supersonic separator are systematically studied and summarized.
- (2) The liquid film's entrainment, the droplets' deposition, and the condensation of water vapor are all calculated as non-negligible items, so the CFD model has a relatively reliable accuracy for separation efficiency evaluation.
- (3) The sensitivity of inlet pressure, heterogeneous droplets' diameter, and inlet droplets' concentration to separation efficiency was analyzed. On this basis, the optimal inlet droplet diameter and concentration are explored for better separation efficiency.

2. Problem statement

2.1. Physical process description

The supersonic separator has both cryogenic refrigeration and gas-water separation functions. Its typical structure is shown in Fig. 1, which is mainly composed of a vortex generator, a supersonic nozzle, a cyclone separator, and a diffuser [31]. The gas-liquid mixture to be separated enters through the inlet of the SS at a certain pressure and flows through the vortex generator to generate a rotating flow field [50]. Then, as it flows through the convergent section of the supersonic nozzle, the rotating flow speeds up while the temperature and pressure drop [51]. When it reaches the nozzle's throat, the mixture would be accelerated to a supersonic speed, and the temperature can be reduced by 50–80 K compared to the inlet. Next, in the divergent section of the nozzle, under the action of the strong swirling flow field, droplets with large inertia are thrown onto the wall and aggregate to form the liquid film [40]. Finally, at the drain outlet, the liquid film and part of the droplets are separated from the liquid outlet while the gas enters the diffuser and exits from the gas outlet. The gas-liquid separation process is achieved [52].

The entire separation process is a complicated three-field two-phase flow in which the liquid phase exists in two forms (droplet and liquid

film). Specifically, the two phases refer to the gas and liquid phase, and the three fields represent the gas, droplet, and liquid film. The complexity is reflected in the mass transfer between the species transport in the gas phase and between the three fields. The evaporation, condensation between the gas and droplets, the evaporation, condensation between the gas and liquid film, and the deposition, entrainment between the droplets and liquid film all would influence the flow field, thus changing the separation efficiency of the supersonic separator [53]. The primary research aim of this paper is to reconstruct these complex physical processes for a supersonic separator using the CFD method.

2.2. Evaluation of separation efficiency

The droplet removal rate η_p , water vapor removal rate η_v , and dew point depression ΔT_d are used to assess the separation efficiency of the supersonic separator. The droplet removal rate η_d refers to the proportion of the droplet mass flow rate separated by the liquid outlet to the droplet inlet mass flow rate, which is calculated as

$$\eta_p = \frac{q_{p, \text{out}}}{q_{p, \text{in}}} \times 100\% \quad (1)$$

The water vapor removal rate η_v evaluates the change of water vapor content in the gas phase after the

Flow passes through the supersonic separator, which could be written as

$$\eta_v = \frac{x_{v, \text{in}} - x_{v, \text{out}}}{x_{v, \text{in}}} \times 100\% \quad (2)$$

where $x_{v, \text{in}}$ is the mole fraction of water vapor at the inlet, and $x_{v, \text{out}}$ is the mole fraction of water vapor at the dry gas outlet.

When the gas pressure and mass fraction of the water vapor are kept constant, the temperature at which water vapor reaches saturation due to the drop in gas temperature is called dew point temperature, or dew point for short. The dew point depression is defined as the difference between the inlet and the dry gas outlet dew point, which is expressed as [54].

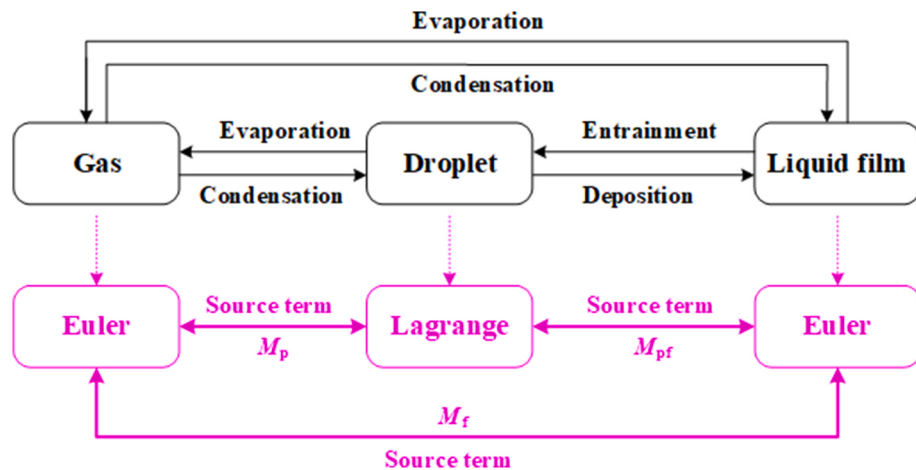


Fig. 3. Correspondence between the established method and three-field two-phase flow.

$$\Delta T_d = T_{d, \text{in}} - T_{d, \text{out}}$$

2.3. Computational domain and meshing

Fig. 2 (a) shows the computational domain of the supersonic separator hired in this paper, where the geometric axis of symmetry is the z-axis. The origin is at the center of the beginning of the blade. The inner and outer diameters of the separator inlet are 27 and 54 mm, and the diameter of the nozzle throat and diffuser outlet are 11.58 and 48.6 mm, respectively. Moreover, the distance from the inlet to the supersonic nozzle is 100 mm. The structured mesh is drawn as shown in **Fig. 2** (b). The grids near the leading and rear edges of the blades and the supersonic nozzle's inlet, throat, and outlet should be refined to ensure the simulation quality. By undertaking a Grid Convergence Index (GCI) test [55], the refined mesh with 557 560 quadrilateral cells was utilized.

3. Mathematical model

The formation and development of liquid film and phase change in three fields were often ignored in the previous numerical studies of the supersonic separator, leading to deviation in the estimation of separation efficiency. Therefore, the Eulerian wall film model was introduced in this paper and coupled with the Eulerian-Lagrangian model. As shown in **Fig. 3**, Euler equations simulate the flow characteristics of the gas phase and liquid film, while the behaviors of droplets are tracked in the Lagrangian coordinate frame. Specifically, the following physical processes are considered in the model:

- (1) Inlet fluid is a mixture of gas, water vapor, and liquid droplets.
- (2) The condensation of the water vapor, the heterogeneous growth of droplets, and the evaporation of droplets are considered. The effect of the foreign droplets on separation efficiency is mainly researched, so homogeneous condensation is reasonably ignored.
- (3) Entrainment, separation, stripping of the liquid film, and deposition of the droplets are considered.
- (4) The interphase mass and heat coupling between the liquid film and the gas phase is taken into account.

3.1. Eulerian-Lagrangian model

The governing equations of the gas phase are expressed in the form of Eq. (4) - Eq. (6):

$$\frac{\partial \rho_g}{\partial t} + \nabla(\rho_g v_g) = S_m \quad (4)$$

(3)

$$\frac{\partial}{\partial t} (\rho_g v_g) + \nabla(\rho_g v_g v_g) = -\nabla p + \nabla \cdot \left[\mu_g \left(\nabla v_g + \nabla v_g^T - \frac{2}{3} \nabla v_g K_r \right) \right] + \rho_g \vec{g} + S_v \quad (5)$$

$$\frac{\partial(\rho_g E)}{\partial t} + \nabla \cdot [v_g (\rho_g E + p)] = \nabla \cdot (-\lambda_{\text{eff}} \nabla T + \tau_{\text{eff}} \cdot v_g) + S_m h_v \quad (6)$$

where ρ_g , v_g are the gas density and velocity. p , T are the pressure and temperature, respectively. ∇ is the surface gradient operator. S_m and S_v are the source terms of mass and momentum. μ_g is the dynamic viscosity. K_r is Kronecker delta number. E is the total enthalpy, and h_v represents the latent heat of the water vapor. λ_{eff} and τ_{eff} are the effective thermal conductivity and effective stress tensor, respectively. h_v is calculated as follows [56]:

$$h_v = h_{v,0} \left(\frac{1 - T/647.3}{1 - 0.5767} \right)^{0.38} \quad (7)$$

where $h_{v,0} = 2262.2 \text{ J kg}^{-1}$. The source terms are composed of two parts, that is

$$S_m = -M_p + M_f \quad (8)$$

$$S_v = -M_p v_p + M_f v_f \quad (9)$$

where M_p and M_f are the mass change rate ($\text{kg m}^{-3} \text{ s}^{-1}$) of gas caused by the evaporation and condensation of the droplets, and the liquid film's phase change, respectively. Furthermore, M_p and M_f are calculated by Eq. (19) and Eq. (25). v_p and v_f represent the velocities of droplet and liquid film.

The species transport equation for the gas phase is expressed as:

$$\frac{\partial}{\partial t} (\rho_g Y_i) + \nabla \cdot (\rho_g v_g Y_i) = -\nabla \cdot \vec{J}_i + S_i \quad (10)$$

where Y_i is the mass fraction of each species, \vec{J}_i represents mass diffusion. S_i is the mass source term of the species.

The trajectory and physical properties of droplets were tracked in the Lagrangian coordinate system. The droplet trajectory equation can be summarized as follows:

$$m_p \frac{dv_p}{dt} = m_p \frac{(v_g - v_p)}{\tau_r} + m_p \vec{g} \quad (11)$$

where m_p is the mass of the droplet. In the supersonic separator, the forces on the droplet are mainly gravity and drag force. In the flow process, physical processes such as condensation, evaporation,

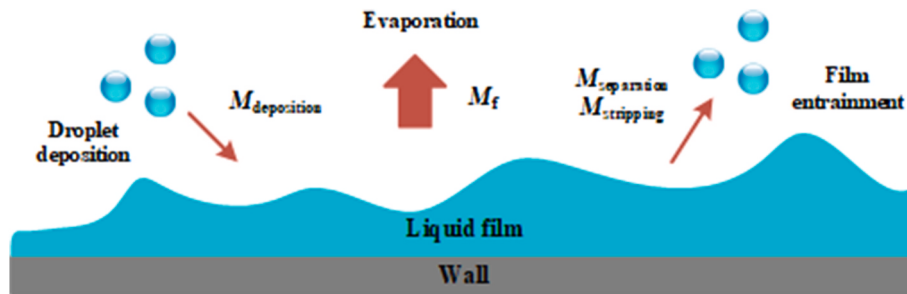


Fig. 4. Schematic of the film mass source terms.

deposition and entrainment will change the droplet diameter and mass. Collision and coalescence between droplets may occur when droplet paths cross, and the effect of such behavior on droplet properties is measured by O'Rourke algorithm [57], which assumes that two droplets can collide only if they move into the same cell.

The droplet relaxation time τ_r can be calculated by Eq. (12):

$$\tau_r = \frac{\rho_p d_p^2 C_c}{18\mu} \quad (12)$$

where d_p , ρ_p are the particle diameter and density, and factor C_c is the Cunningham correction to Stokes' drag law [58], which is defined as:

$$C_c = 1 + \frac{2\lambda_{mg}}{d_p} \left(1.257 + 0.4e^{-\frac{1.1d_p}{2\lambda_{mg}}} \right) \quad (13)$$

where λ_{mg} is the mean free path of a gas molecule.

The sound speed in gas-liquid two-phase separation is calculated by Wood's law [59, 60]:

$$c_{g-l} = \sqrt{\frac{1}{(\alpha_g K_g^{-1} + \alpha_l K_l^{-1})(\rho_g \alpha_g + \rho_l \alpha_l)}} \quad (14)$$

where α_g , α_l are volume fractions of gas and liquid, and K is the bulk elastic modulus.

3.2. Eulerian wall film model

The Eulerian wall film model is used here to simulate the behavior of liquid film. Since the liquid wall film is often very thin [61], it is important to note that the flow perpendicular to the wall of the supersonic separator can legitimately be ignored in the Eulerian wall film model. The mass balance equation for the liquid film is

$$\frac{\partial \rho_f \delta}{\partial t} + \nabla \cdot (\rho_f \delta v_f) = \delta (M_{pf} - M_f) \quad (15)$$

where ρ_f , δ are the film density and thickness, M_{pf} is the mass source term between droplets and liquid film [62], and the physical meanings of M_f and M_{pf} can be obtained from Fig. 4.

Conservation of film momentum is given as

$$\frac{\partial \rho_f \delta v_f}{\partial t} + \nabla \cdot (\rho_f \delta v_f v_f) = -\delta \cdot \nabla P_L + \delta \rho_f \vec{g}_\tau + \frac{3}{2} \tau_{f-g} - \frac{3\mu_f}{\delta} v_f + \delta (M_{pf} - M_f) v_f \quad (16)$$

$$P_L = p_g - \underbrace{\rho \delta (\vec{n} \cdot \vec{g})}_{P_h} - \underbrace{\sigma \nabla \cdot (\nabla \delta)}_{P_\sigma} \quad (17)$$

where \vec{g}_τ is the gravity component parallel to the film, τ_{f-g} is the viscous shear stress on gas-film interfaces, μ_f is the dynamic viscosity of film.

The liquid film governing equations of energy is described as

$$\frac{\partial}{\partial t} (\rho_f \delta h_f) + \nabla \cdot (\rho_f \delta h_f v_f) = \frac{\lambda_f}{\delta} (T_s + T_w - 2T_m) + \delta (M_{pf} - M_f) h_v \quad (18)$$

where h_f is the enthalpy of film, T_s , T_w , and T_m are the temperature of the film surface, wall, and film half-depth, respectively.

3.3. Three-field mass and heat transfer interactions

There are three main aspects of the three-field heat and mass exchange in the supersonic separator. The first is the evaporation and condensation between gas and droplets. The second is the phase change between gas and liquid film. The third is the deposition and entrainment between droplets and liquid film.

3.3.1. Heterogeneous droplet condensation model

The two-way coupling method is adopted to calculate the mass exchange between the gas phase and the droplet. M_p in Eq. (8) can be calculated as follows:

$$M_p = A_p \rho_p \frac{dr_p}{dt} \quad (19)$$

where A_p is the surface area of the droplet, r_p is the radius of the droplet, and the growth rate of the droplet is expressed as

$$\frac{dr_p}{dt} = \frac{\sum_{i=1}^2 v_i}{\rho_p h_v} (T_r - T_v) \quad (20)$$

The heat transfer coefficient v_i is written as [63].

$$v_i = \left(2 + 0.6 \text{Re}^{1/2} \text{Pr}_g^{1/3} \right) \frac{\lambda_i}{2r_p} \frac{1}{1 + \frac{4\sqrt{2\pi}}{1.5\text{Pr}_g} \times \frac{r_i}{1+r_i} K_n} \quad (21)$$

where the subscript i represents different species in the gas phase. λ , Re, Pr, K_n , and Γ are the thermal conductivity, Reynolds number, Prandtl number, Knudsen number, and specific heat ratio.

And T_r in Eq. (20) denotes the droplet surface temperature, which can be calculated by [64].

$$T_r = T_d - \frac{r_c}{r_p} (T_d - T_g) \quad (22)$$

where r_c is the critical nucleation radius of the droplet, and the calculation equation for r_c is

$$r_c = \frac{2\sigma}{\rho_p R_v T_v \ln(S_s)} \quad (23)$$

where R_v represents a specific gas constant of water vapor, and T_v is water vapor temperature. S_s means supersaturation, equals $p_v/p_s(T_g)$, and p_s is the water vapor saturation pressure at temperature T_g . σ is the liquid surface tension (N m^{-1}), which is calculated by

$$\sigma = (85.27 + 75.612 T_R - 256.889 T_R^2 + 95.928 T_R^3) \times 10^{-3} \quad (24)$$

where T_R ($T_R = T_g/T_c$) is the reduced temperature, and T_c is the critical temperature (647.3 K).

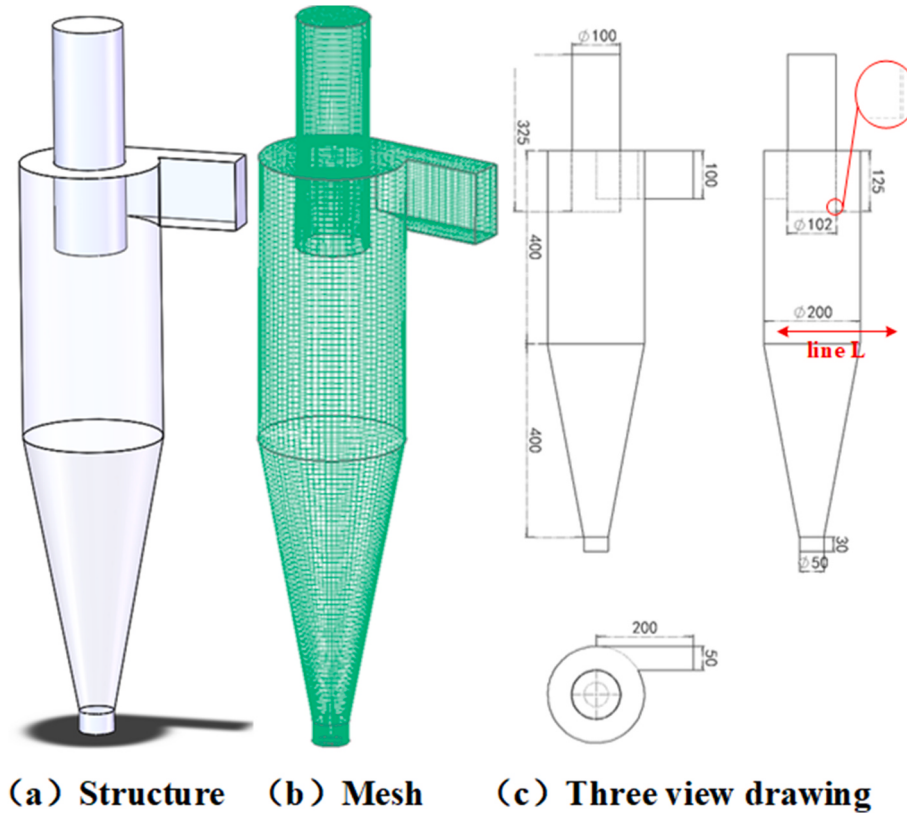


Fig. 5. Structure, mesh, and size of the cyclone separator.

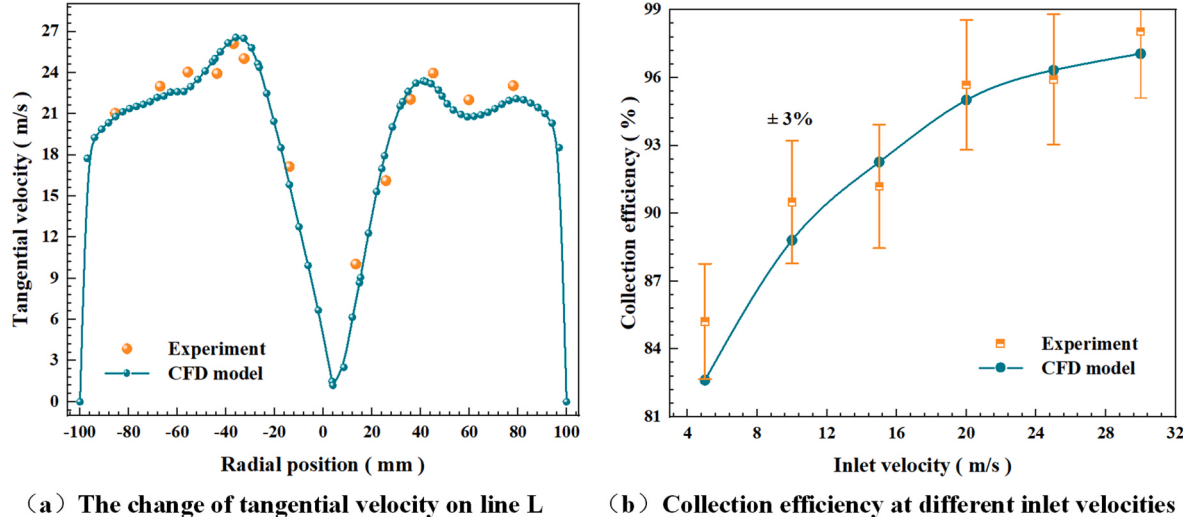


Fig. 6. Comparison between experimental and CFD model's results for the cyclone separator.

3.3.2. Gas film phase change model

The species transport model can analyze the phase changes between film material (liquid) and the gas species (water vapor) in the flow process when coupled with the film Model. That is, the calculation equation for M_f is as follows [65]:

$$\delta M_f = \frac{(\rho_m D_v / \delta)}{\rho_m D_v / \delta + C_{\text{phase}}} C_{\text{phase}} (y_{\text{sat}} - y_i) \quad (25)$$

$$C_{\text{phase}} = \begin{cases} C_{\text{con}}, & y_i > y_{\text{sat}} \\ C_{\text{evap}} \cdot 10^4, & y_i < y_{\text{sat}} \end{cases} \quad (26)$$

where ρ_m is the density of the gas mixture, D_v ($\text{m}^2 \text{s}^{-1}$) is the mass diffusivity of the vapor species, C_{phase} is the phase change constant, C_{con} and C_{evap} ($\text{kg m}^{-2} \text{s}^{-1}$) are condensation and evaporation constant (10^{10}) [66], the film height δ is used to prevent generating vapor without the presence of liquid. y_i represents the mass fraction of the species. It is clear from Eq. (25) that when the vapor mass fraction exceeds the saturation mass fraction, condensation occurs (negative M_f). The saturation species mass fraction y_{sat} is computed as:

$$y_{\text{sat}} = \frac{p_{\text{sat}}(T)}{\rho_m} \frac{Mw_i}{Mw_m} \quad (27)$$

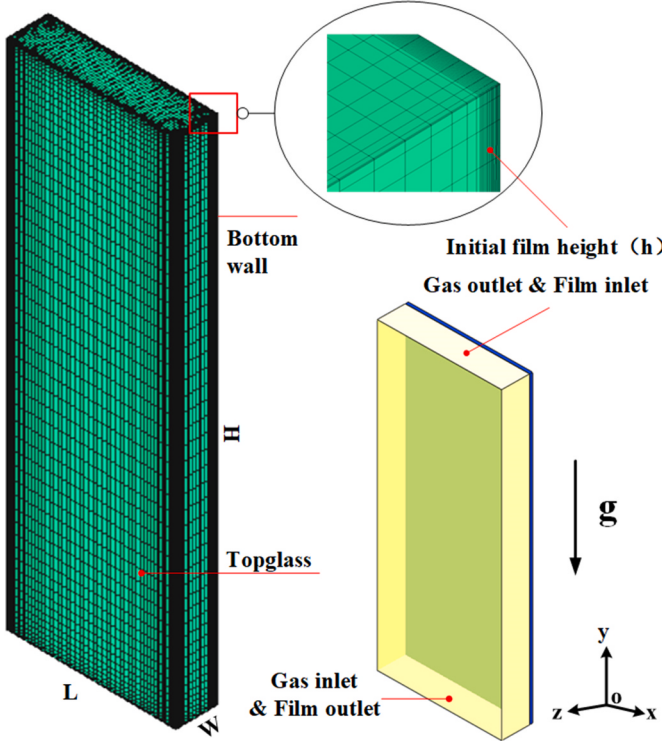


Fig. 7. Structure and mesh of the rectangular channel.

where P_m is the absolute pressure of the gas mixture, Mw_i and Mw_m are the molecular weight of the species and the mixture, respectively. p_{sat} is only related to temperature. In this paper, the species is considered as water vapor, and its saturation pressure is calculated as [67]:

$$\log_{10} p_{\text{sat}} = -2.1794 + 0.02953 \times T - 9.1837 \times 10^{-5} \times T^2 + 1.4454 \times 10^{-7} \times T^3 \quad (28)$$

3.3.3. Droplet deposition and liquid film entrainment model

As shown in Fig. 4, M_{pf} in Eq. (15) mainly consists of the deposition of droplets and the separation and stripping of the liquid film. The expression of M_{pf} is:

$$M_{\text{pf}} = M_{\text{deposition}} - M_{\text{separation}} - M_{\text{stripping}} \quad (29)$$

Droplet deposition will occur when a droplet hits the wall with high enough energy and is absorbed into the film surface, and $M_{\text{deposition}}$ represents the mass exchange of this part. $M_{\text{separation}}$ is the mass source contributed by liquid film separation, which occurs near the separation port of the supersonic separator when the following two conditions are met:

$$\theta > \theta_c, We_f > We_c \quad (30)$$

where θ is the separation angle of the liquid outlet, We_f is the Weber

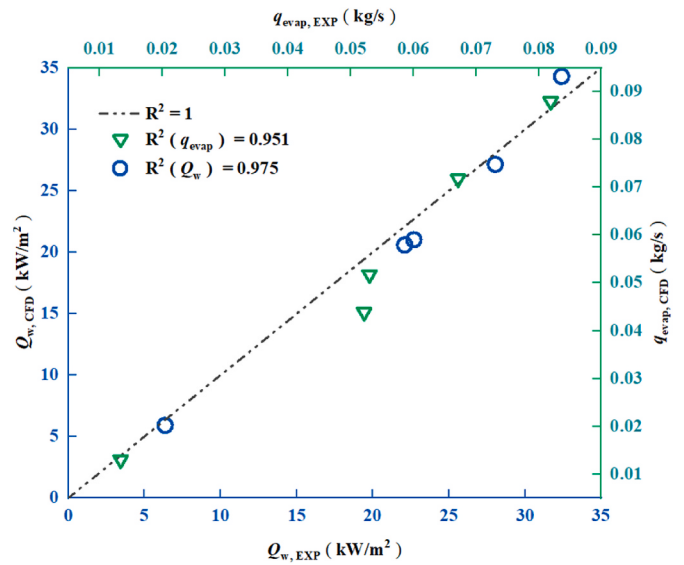


Fig. 9. R Square of q_{evap} and Q_w obtained from the experiment and CFD model.

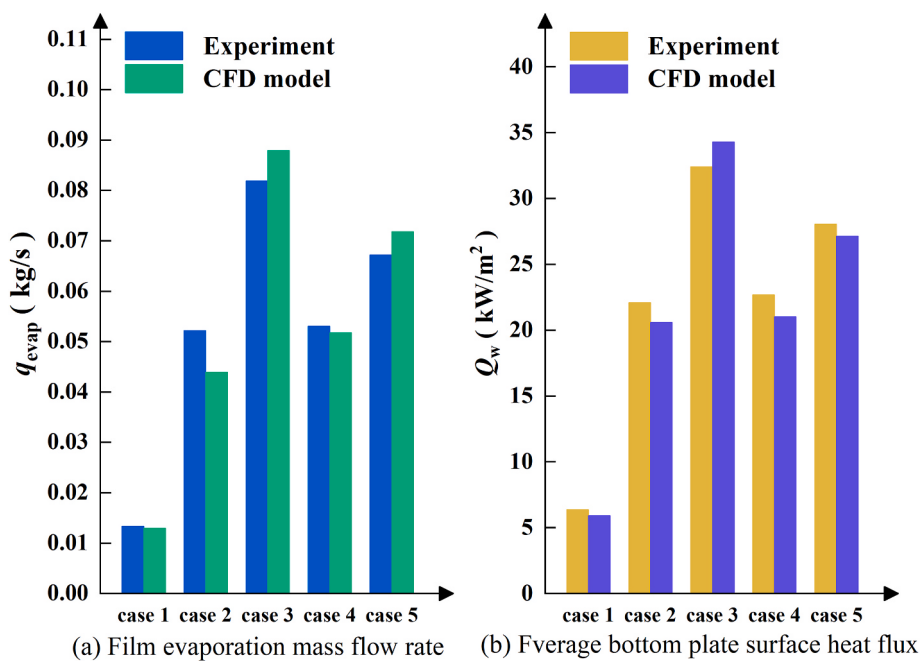


Fig. 8. The liquid film evaporation mass flow rate and the average bottom plate surface heat flux obtained from the experiment and CFD model.

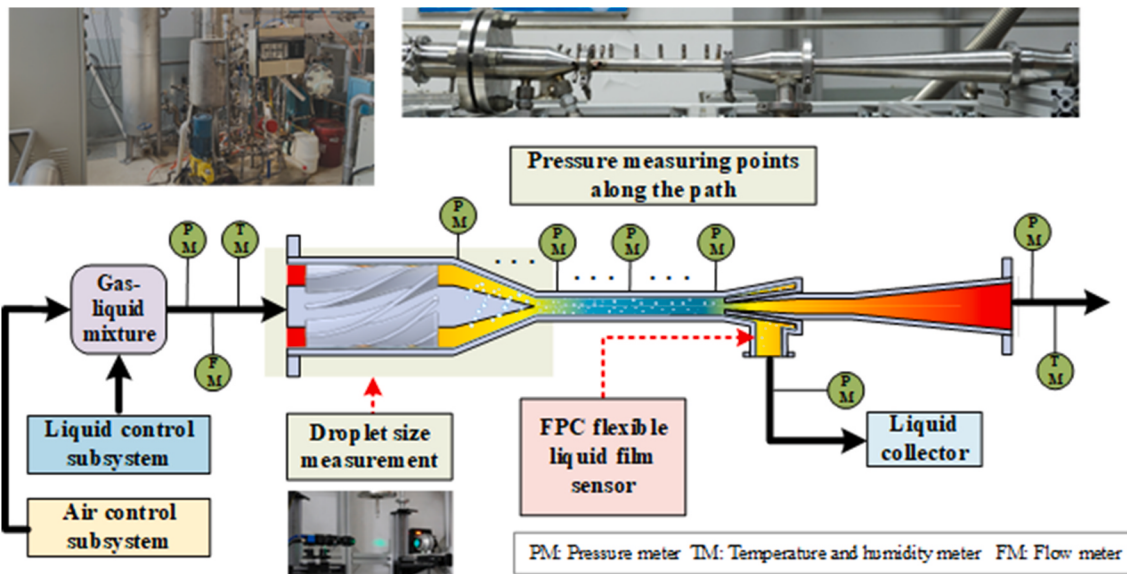


Fig. 10. Experimental process and equipment.

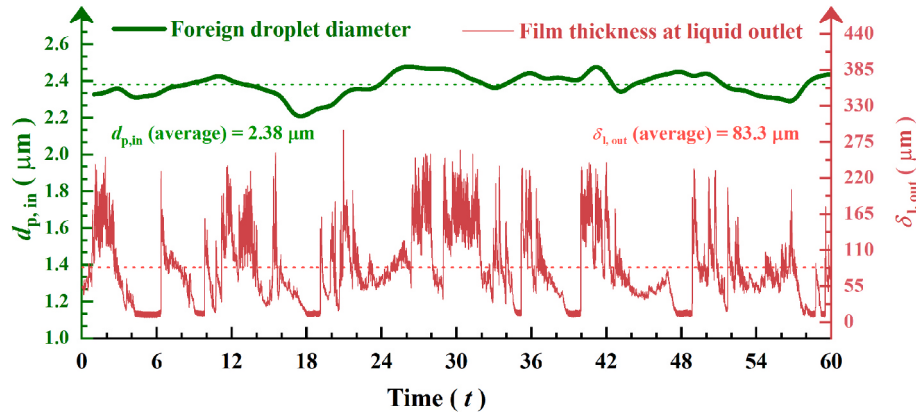


Fig. 11. Measurement of foreign droplets' diameter and film thickness at the liquid outlet.

Table 1
Experiment data of pressure along the wall surface of the supersonic nozzle.

Measuring position (mm)	-50	-34.8	-19.2	-0.5	1.2	2	30	34.6
Measured pressure (atm)	3	2.954	2.921	1.812	1.755	1.469	1.647	1.594
Pressure ratio	1	0.984	0.974	0.604	0.585	0.490	0.550	0.531
Measuring position (mm)	43.8	48.7	61.3	105.8	148.5	189.5	229.2	249.2
Measured pressure (atm)	1.509	1.423	1.304	1.155	0.992	0.850	0.818	0.740
Pressure ratio	0.503	0.474	0.435	0.385	0.331	0.283	0.273	0.247

number based on the film, and subscript c represents a critical value. We_f is calculated by

$$We_f = \frac{\rho_f \delta |v_f|^2}{\sigma} \quad (31)$$

The Foucart model for edge separation assumes that the separation droplet diameter is given by

$$d_{\text{separation}} = \left(\frac{3\delta^2 l}{4\pi} \right)^{\frac{1}{3}} \quad (32)$$

where l is the length of the edge. $M_{\text{separation}}$ can be calculated as

$$M_{\text{separation}} = \frac{v_f \hat{n}_e \delta \rho_f}{V_{\text{cell}}} \quad (33)$$

where \hat{n}_e is the inward pointing normal from the edge centroid to the face center.

When the relative velocity between the gas core on the wall and the liquid film is high, that is, at a sufficiently high shear rate, Kelvin-Helmholtz waves form and grow on the film surface, eventually stripping droplets from the surface. This process is called film stripping, and the wave frequency (ω) is defined by

$$\omega = 0.384 \sqrt{\frac{\rho_g}{\rho_f}} \frac{\rho_g v_g^3}{\sigma} \quad (34)$$

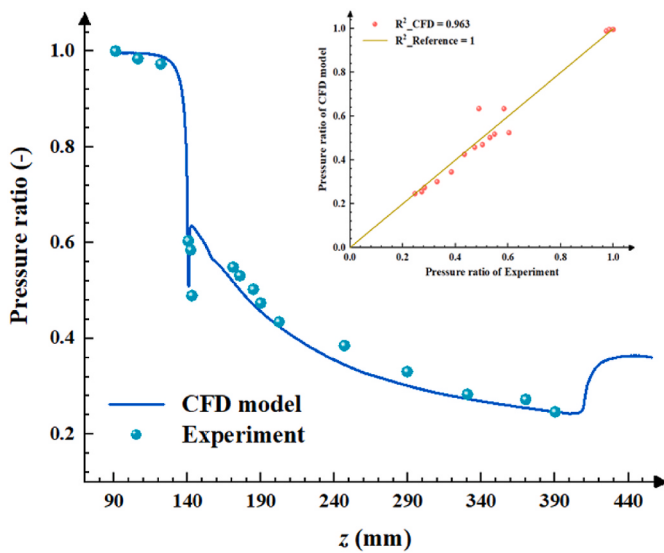


Fig. 12. Pressure distribution along the wall surface of the supersonic nozzle.

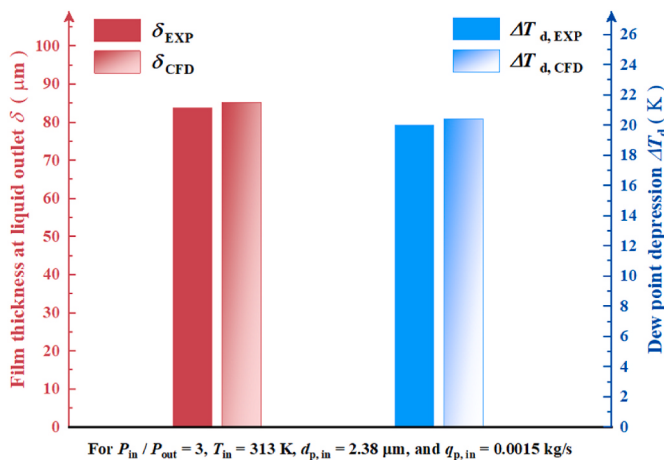


Fig. 13. Values of liquid film thickness at liquid outlet and dew point depression.

Furthermore, the average stripping droplet diameter and mass change of the stripping droplet $M_{\text{stripping}}$ are determined by the following equations:

$$\bar{d}_{\text{stripping}} = F \cdot 9 \cdot \sqrt[3]{16} \cdot \pi \left(\frac{\mu_f \sqrt{\sigma/\rho_f}}{\beta \rho_g v_g^2} \right)^{2/3} \quad (35)$$

$$M_{\text{stripping}} = \frac{C \cdot 9 \cdot \sqrt[3]{16} \cdot \pi \omega \rho_f}{V_{\text{cell}}} \left(\frac{\mu_f \sqrt{\sigma/\rho_f}}{\beta \rho_g v_g^2} \right)^{2/3} \quad (36)$$

where F and C are the diameter coefficient (0.14) and mass coefficient (0.5). β is a sheltering parameter (0.3).

3.4. Solution strategy

The pressure inlet and outlet are used as the inlet and outlet boundary conditions. The inlet temperature and relative humidity are set to be 300 K and 100%. The discrete droplets are released at the inlet, and their initial velocity is consistent with the gas phase. The foreign droplets' initial diameter and mass flow rate can be specified. When the droplet impacts a wall, it will be collected into a liquid film, break up or

bounces off. When the droplet moves to the gas outlet, it is considered to escape. Collision and coalescence between droplets are also taken into account.

All the cases were simulated by ANSYS FLUENT, and the User-Defined-Scalar (UDS) and User-Defined-Function (UDF) were hired to calculate the heterogeneous condensation of the droplets and the source term in the governing equations. The transient pressure-based solver was used to calculate the governing equations of the three fields. The RSM turbulence model was employed for its high precision in swirling problems [68]. The SIMPLE algorithm was utilized for the coupling of velocity and pressure fields. The second-order upwind scheme was adopted to discretize the governing equations, turbulence kinetic energy equation, and turbulent dissipation rate equation.

4. Model validation

The effectiveness of the established model was validated by the following three aspects: the validation of the strong rotational flow model, the validation of the liquid film model, and the validation of the three-field two-phase model.

4.1. Validation of the strong rotational flow model

The droplet model was validated by simulating the separation process in a cyclone separator according to the experimental data of Wang et al. [69]. Similar to the supersonic separator, the strong rotational forces generated inside the cyclone separator can throw the large inertia particles to the wall, where they are eventually collected at the particle outlet. The structure and size of the cyclone separator are shown in Fig. 5 (a) and Fig. 5 (c), where the gas flows to the top, and the particles move to the bottom. The diameters of the gas outlet and particle outlet are 100 mm and 50 mm, respectively, and the inlet is a rectangular section of 100 mm long and 50 mm wide. The gravity direction of the cyclone separator is the negative Y-axis. Fig. 5 (b) is a structured mesh drawn according to the geometry. By GCI test, a grid size of 235031 ensured the grid-independent solution. Fig. 6 (a) shows the experimental and simulated tangential velocity distribution on line L when the inlet velocity is 20 m/s. Both the distribution rules and numerical dimensions of the two are consistent. Fig. 6 (b) compares the numerical and experimental results of collection efficiency at different inlet velocities, and the error between them is less than $\pm 3\%$. The above results validate that the proposed model can maintain high accuracy in the simulation of particle behavior in strong rotational flow.

4.2. Validation of the liquid film model

The liquid film model was validated refer to the experiment of Du et al. [70]. As shown in Fig. 7 (left), the rectangular channel comprises a steel plate at the bottom, a glass cover plate at the top, and steel walls at the left and right sides. The channel's height is 5.0 m and the channel is perpendicular to the XOZ plane. The inlet and outlet of the channel are rectangular areas with a length of 1.2 m and a width of 0.3 m. The inlet section of the gas phase is the outlet section of the liquid film, which means that the liquid film moves on the negative Y-axis under the force of gravity. Air flows into the calculation domain from the bottom of the channel and forms a countercurrent with the liquid film. The initial film thickness h is 0.01 m, and the film width is 1.2 m, covering the whole bottom steel plate. The structured mesh is shown in Fig. 7 (right). The mesh near the wall is refined. The bottom plate area where the liquid film flows, having a significant influence on the flow results, is also refined. By GCI test, a mesh size of 960687 ensured a grid-independent solution.

Fig. 8 compares the numerical and experimental value of liquid film evaporation mass flow rate and the average bottom plate surface heat flux under different conditions. The two values are in good agreement. R^2 (R Square) is used to evaluate the consistency, which can be calculated

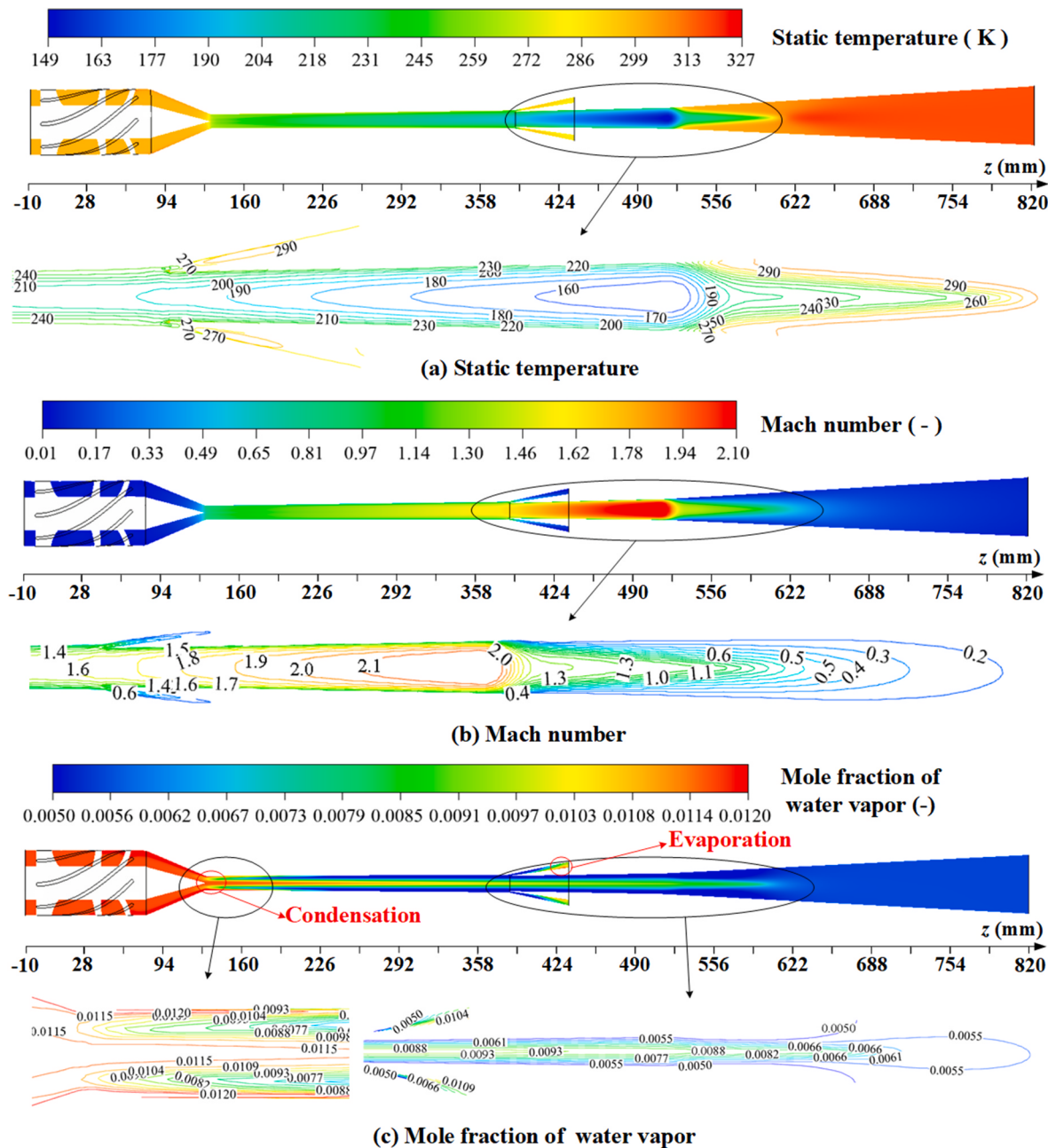


Fig. 14. Flow parameter profiles of the gas phase in supersonic separator when $d_{p, \text{in}} = 2.2 \mu\text{m}$, $q_{p, \text{in}} = 0.001 \text{ kg/s}$ and $p_{\text{in}} = 3 \text{ atm}$.

as:

$$R^2 = 1 - \frac{\sum_{i=1}^n (a_i - b_i)^2}{\sum_{i=1}^n (a_i - \bar{a})^2} \quad (37)$$

where a_i , b_i and \bar{a} are experimental values, CFD values, and experimental sample mean, respectively, and n is the number of experiments. Fig. 9 plots the R Square values, where the R Square of liquid film evaporation mass flow rate is $R^2(q_{\text{evap}}) = 0.951$ and the R Square of the average bottom plate surface heat flux is $R^2(Q_w) = 0.975$. The results indicate that the thermal and mass characteristics between the CFD model and experiment correspond well. The established liquid film model can reasonably predict liquid film's evaporation and heat exchange.

4.3. Validation of the three-field two-phase model in a supersonic separator

The experiments of the supersonic separator shown in Fig. 2 were carried out to validate the prediction ability of the established model for the three-field two-phase flow. The experimental process, equipment, and the actual supersonic separator are shown in Fig. 10. A set of experiments is carried out. The inlet pressure is controlled at 3 atm, the inlet temperature is 313 K, the inlet liquid mass flow rate is 0.0015 kg/s, the relative inlet humidity is 100%, and the outlet pressure is 1 atm. Pressure, temperature, humidity and flow measurement devices are arranged at the inlet and outlet of the supersonic separator. The values of inlet foreign droplet diameter $d_{p, \text{in}}$, the film thickness at the liquid outlet $\delta_{l, \text{out}}$, and the pressure distribution along the wall surface were measured by an optical instrument, FPC flexible liquid film sensor, and pressure probes.

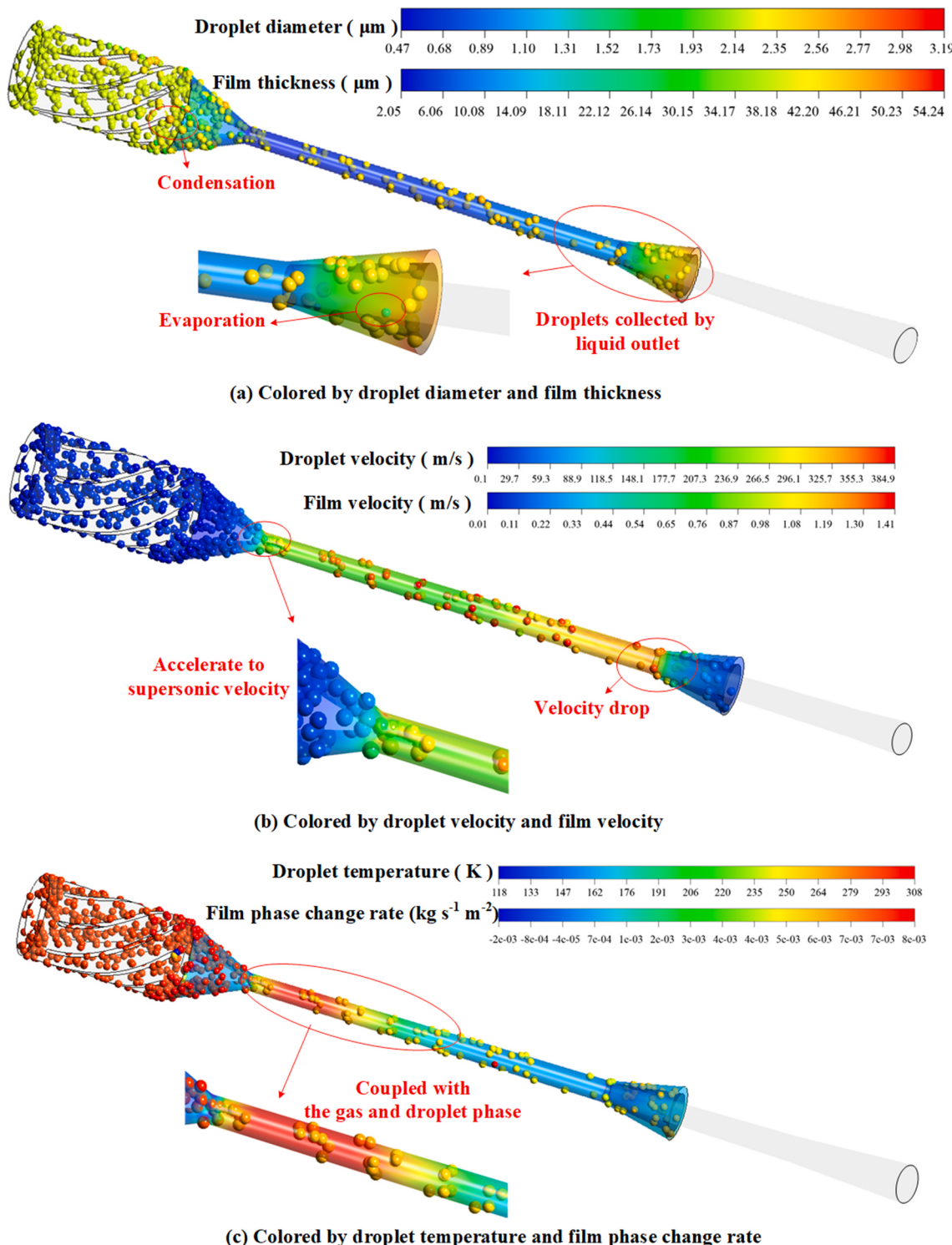


Fig. 15. Droplet motion and liquid film formation characteristics when $d_{p,\text{in}} = 2.2 \mu\text{m}$, $q_{p,\text{in}} = 0.001 \text{ kg/s}$ and $p_{\text{in}} = 3 \text{ atm}$.

Fig. 11 shows the changes in $d_{p,\text{in}}$ and $\delta_{l,\text{out}}$ in a period. It can be found that the average droplet diameter at the inlet is $2.38 \mu\text{m}$, and the average film thickness at the liquid outlet is $83.3 \mu\text{m}$. The specific data of the pressure along the path can be obtained from Table 1. Next, the established CFD model was used for simulation. The geometric size and structured mesh of the supersonic separator used in the simulation are shown in Fig. 2. The experimental conditions were taken as CFD conditions. The diameter of the inlet droplet was set as $2.38 \mu\text{m}$, and corresponding CFD results were obtained. The pressure distribution along

the wall surface of the supersonic nozzle between the experiment and the CFD model is compared in Fig. 12 (main graph). It can be seen that there is a good correspondence between the two, and the value of R Square reaches 0.963 (Fig. 12 (subgraph)). Fig. 13 shows the different performances of liquid film thickness and dew point depression under the experimental and CFD results. The dew point depression is calculated from the temperature and humidity data at the inlet and outlet. The experimental and CFD values are consistent. Therefore, reasonable results can be obtained through the established CFD model for modeling

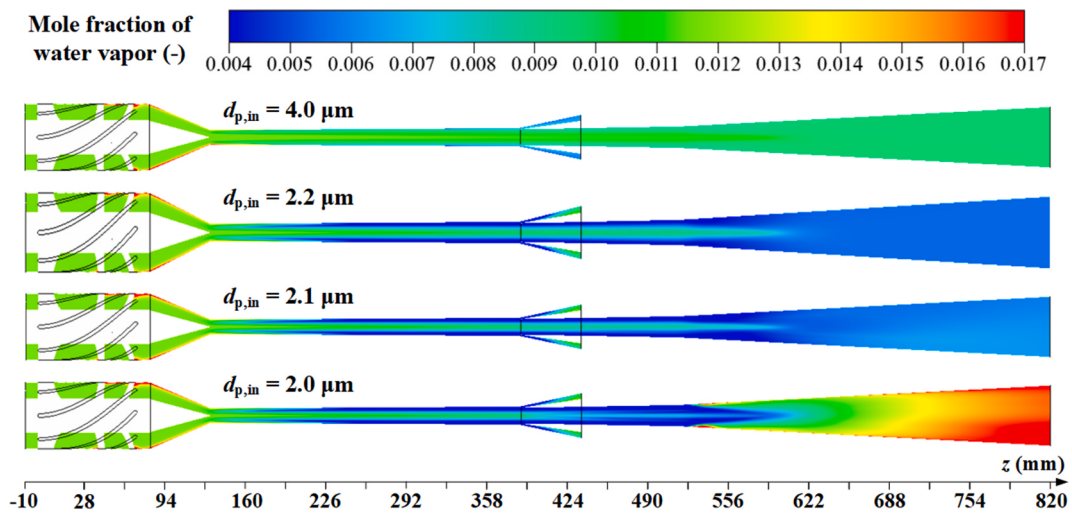


Fig. 16. Mole fraction of water vapor of the first group when $q_{p,in} = 0.001 \text{ kg/s}$ and $p_{in} = 3 \text{ atm}$.

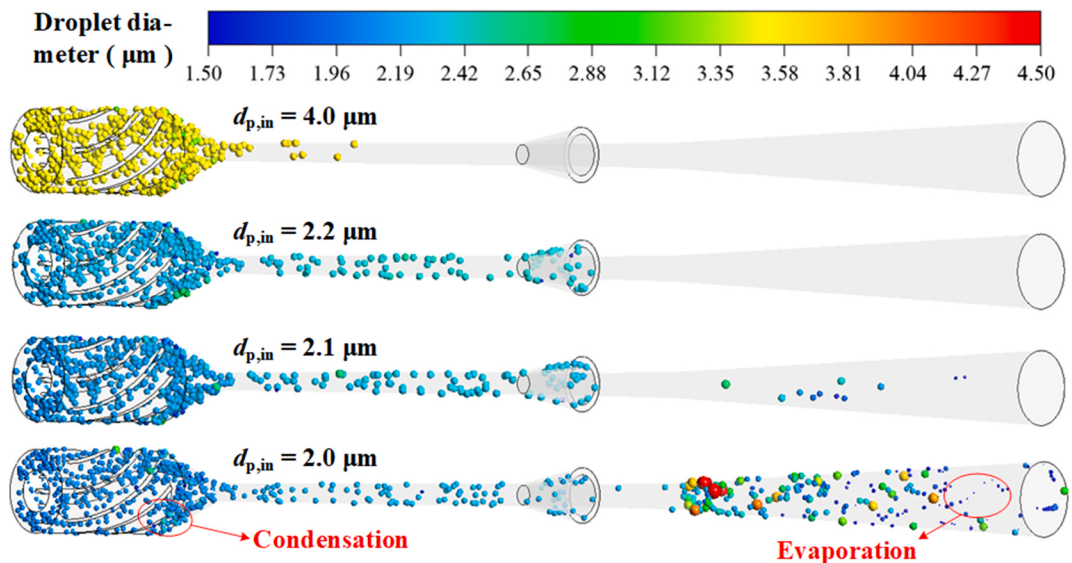


Fig. 17. Droplet trajectory of the first group when $q_{p,in} = 0.001 \text{ kg/s}$ and $p_{in} = 3 \text{ atm}$.

the three-field two-phase flow in the supersonic separator.

5. Results and discussion

The above three experimental validations prove that the established mathematical model can effectively simulate the characteristics of three-field two-phase flow in the supersonic separator. In this chapter, the gas, droplet, and liquid film behaviors in the supersonic separator are studied using the proposed three-field two-phase flow model. Then the influence of inlet conditions on the heat and mass characteristics of the supersonic three-field two-phase flow is analyzed. Furthermore, the way to improve separation efficiency in the supersonic separator is explored.

5.1. Characteristic analysis of gas, droplet, and liquid film

Under a typical condition that T_{in} (inlet temperature) = 300 K, p_{in} (inlet pressure) = 3 atm, p_{out} (outlet pressure) = 1 atm, $d_{p,in}$ (inlet droplet diameter) = 2.2 μm and $q_{p,in}$ (inlet droplet mass flow rate) = 0.001 kg/s, the static temperature and Mach number distribution of cross-section $y = 0 \text{ mm}$ in the designed supersonic separator are shown in Fig. 14 (a) and Fig. 14 (b). The gas is continuously compressed in the

convergent section of the supersonic nozzle, which leads to a decrease in static temperature and an increase in Mach number. When the gas moves to the throat of the supersonic nozzle, the Mach number reaches 1, and accordingly, the static temperature decreases by at least 60 K. Then, the supersonic gas will continue to pass through the divergent section of the supersonic nozzle and the diffuser, with the continuous increase of Mach number. When the Mach number reaches a maximum of 2.1, the temperature has dropped to a minimum of 149 K.

The cooling process turns the nozzle divergent section of the supersonic separator into a low-temperature environment and promotes the condensation of water vapor in the gas phase. Fig. 14 (c) is the mole fraction distribution of the water vapor of cross-section $y = 0 \text{ mm}$. It can be seen that the mole fraction of water vapor drops significantly after the throat of the supersonic nozzle, which corresponds to an intense condensation in the supersonic separator. Note that since the influence of heterogeneous condensation is mainly considered, condensation also occurs in the convergent of the supersonic nozzle. The condensation process continues to the middle of the diffuser, with the mole fraction of the water vapor reduces to 0.0050 at the minimum. In the middle and back of the diffuser, the pressure and temperature rise of the gas flow inhibits the condensation process. Then evaporation becomes the main

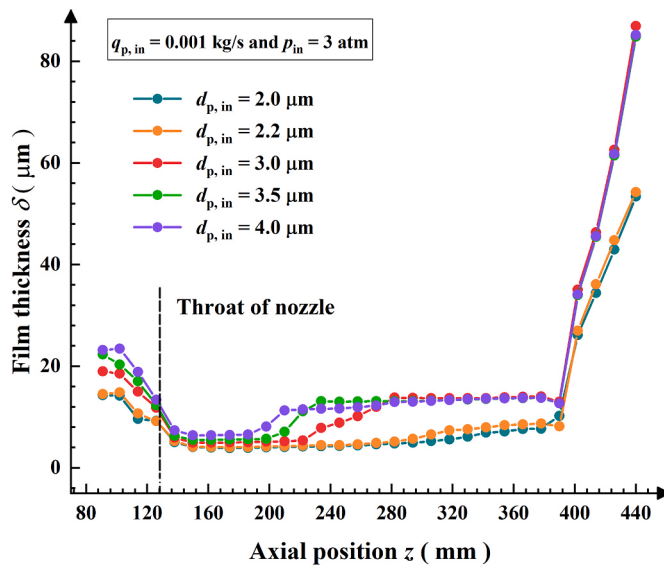


Fig. 18. Film thickness distributions of the first group when $q_{p,\text{in}} = 0.001 \text{ kg/s}$ and $p_{\text{in}} = 3 \text{ atm}$.

mass transfer behavior in the supersonic separator, and the mole fraction of water vapor also rises.

The droplet behavior in the three-field two-phase flow can be captured in Fig. 15. In the case of $d_{p,\text{in}} = 2.2 \mu\text{m}$ and $q_{p,\text{in}} = 0.001 \text{ kg/s}$, the droplets are all thrown to the wall and separated from the liquid outlet. If the inlet conditions change, the droplet separation behavior will be different. In addition, consistent with the behavior of the gas phase, the droplet velocity and temperature show a trend of first increasing and then decreasing. Furthermore, Fig. 15 (a) draws the liquid film thickness distribution on the supersonic separator's wall surface. Through visual analysis, the evolution process of the liquid film can be divided into four stages: Formation stage, acceleration stage, development stage, and deceleration stage. After passing through the cyclone generator, gas with swirling droplets meets the nozzle convergent section, and the swirling droplets start to move to the wall under the action of centrifugal force. The liquid film begins to form at the formation stage. At the acceleration stage, the rapid growth of the gas velocity leads to an increase in droplet and liquid film velocity, as shown in Fig. 15 (b). However, even though the gas velocity has increased to

supersonic, the liquid film attached to the wall has only been accelerated to 0.54 m/s at the nozzle throat. The high shear force between the gas and liquid film will peel off part of the liquid film, which results in the acceleration of the film thickness. In the divergent section of the nozzle, the droplet deposition process is stronger than the stripping process of the liquid film; water vapor also condenses to form liquid film; thus, the liquid film increases slowly, called the development stage. After the film enters the liquid outlet, a diffuser, the effect of gas on liquid film is reduced. The film velocity will slow down, and thickness will sharply rise, although the liquid film's evaporation behavior exists in this deceleration stage.

The liquid film phase change rate distribution is shown in Fig. 15 (c). A value of negative means that water vapor condenses into the liquid film. The condensation area is mainly concentrated in the acceleration and development stages of liquid film thickness, and the evaporation area is distributed in the deceleration stage of the liquid film. The maximum condensation and evaporation film phase change rates are $-2 \times 10^{-3} \text{ kg s}^{-1} \text{ m}^{-2}$ and $8 \times 10^{-3} \text{ kg s}^{-1} \text{ m}^{-2}$, respectively.

5.2. Sensitivity analysis of the inlet characteristics

The influences of the inlet foreign droplets' diameter $d_{p,\text{in}}$, the inlet droplet concentration $q_{p,\text{in}}$, and the inlet pressure p_{in} on the flow characteristics of three-field two-phase condensation are discussed in this section. Three groups of comparative simulations were carried out, as shown below.

5.2.1. Effect of inlet droplet diameter

The inlet droplet diameter is changed in the first group of tests. Fig. 16 and Fig. 17 show the changes in water vapor mole fraction on cross-fraction $y = 0 \text{ mm}$ and the droplet trajectory under different diameters. It can be seen that with the increase of inlet droplet diameter, the mole fraction of water vapor at the gas outlet increases. When $d_{p,\text{in}} = 2.0 \mu\text{m}$ and $2.1 \mu\text{m}$, the mole fraction of water vapor decreases first and then rises. This phenomenon is because some droplets are not centrifuged to the liquid outlet. The unseparated droplets enter the diffuser and evaporate in the secondary diffuser, increasing the mole fraction of water vapor. When $d_{p,\text{in}} = 2.2 \mu\text{m}$ and $4.0 \mu\text{m}$, the mole fraction of water vapor decreases gradually along the axial direction, indicating no droplet evaporation and all droplets are separated.

Moreover, to observe the liquid film distribution, axial distribution data of film thickness under different inlet diameters are collected and plotted in Fig. 18. The liquid film distribution of all conditions conforms

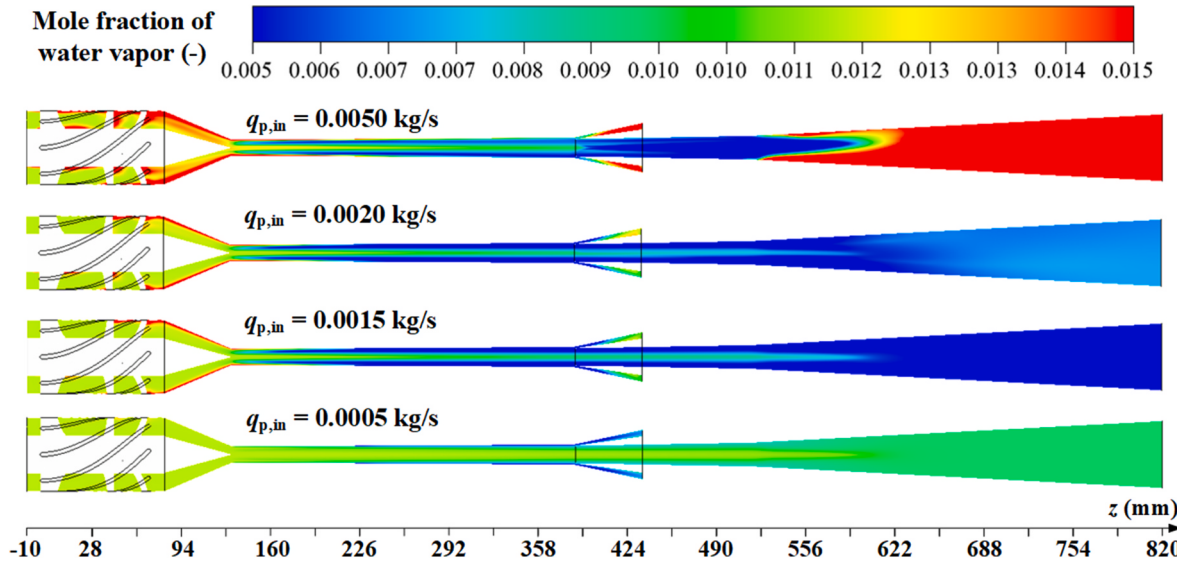


Fig. 19. Mole fraction of water vapor of the second group when $d_{p,\text{in}} = 2.2 \mu\text{m}$ and $p_{\text{in}} = 3 \text{ atm}$.

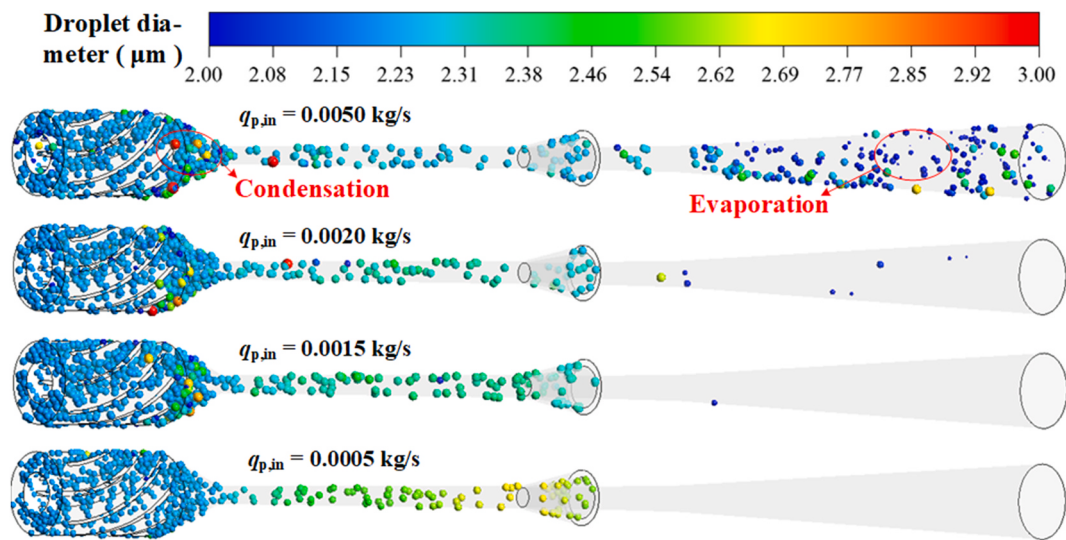


Fig. 20. Droplet trajectory of the second group when $d_{p,\text{in}} = 2.2 \mu\text{m}$ and $p_{\text{in}} = 3 \text{ atm}$.

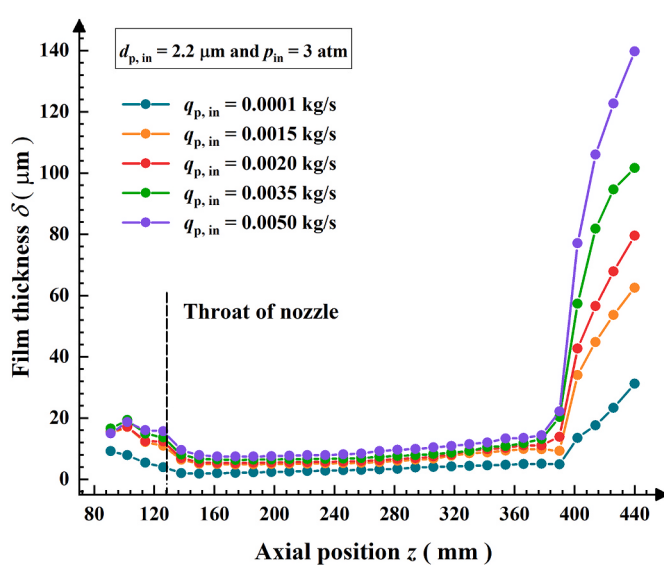


Fig. 21. Film thickness distributions of the second group when $d_{p,\text{in}} = 2.2 \mu\text{m}$ and $p_{\text{in}} = 3 \text{ atm}$.

to the four stages described in section 5.1. It reveals that the larger $d_{p,\text{in}}$ is, the thicker the overall film thickness is, and the higher the liquid outlet's film thickness is. Furthermore, when the inlet particle size increases, the onset position of the development stage will change closer to the nozzle throat. This is because the larger $d_{p,\text{in}}$ is, the earlier the droplets are collected by the wall, that is, the closer the deposition onset location is to the throat. However, due to the same inlet concentration used in this group of tests, when all droplets are separated ($d_{p,\text{in}} > 2.2 \mu\text{m}$), the film thickness at the liquid outlet will not change significantly and will be stable at about 85.2 μm .

5.2.2. Effect of inlet droplet concentration

Keep $d_{p,\text{in}} = 2.2 \mu\text{m}$ and $p_{\text{in}} = 3 \text{ atm}$, the inlet droplet mass flow rate $q_{p,\text{in}}$ was changed in the second group of tests. The water vapor mole fraction at $y = 0 \text{ mm}$ was obtained and shown in Fig. 19. When $q_{p,\text{in}} = 0.0020 \text{ kg/s}$ and 0.0050 kg/s , droplet evaporation occurs in the diffuser. The droplet diameter distribution of different $q_{p,\text{in}}$ is shown in Fig. 20. When $q_{p,\text{in}} = 0.0050 \text{ kg/s}$, a large number of droplets enter the diffuser and evaporate. When $q_{p,\text{in}}$ is reduced to 0.0020 kg/s , a small number of

droplets still enter the diffuser, and the droplets cannot be completely separated. Therefore, proper inlet droplet concentration can better play the performance of the supersonic separator.

The change of liquid film in the second group can be seen in Fig. 21. The liquid film in the supersonic separator experienced a process of formation, acceleration, development, and then sharp increase. The increase of $q_{p,\text{in}}$ will lead to an increase in the overall liquid film thickness. In the deceleration stage, A large mass flow rate corresponds to a large growth range of liquid film. The film thickness at the liquid outlet for $q_{p,\text{in}} = 0.0001 \text{ kg/s}$, $q_{p,\text{in}} = 0.0015 \text{ kg/s}$, $q_{p,\text{in}} = 0.0020 \text{ kg/s}$, $q_{p,\text{in}} = 0.0035 \text{ kg/s}$, and $q_{p,\text{in}} = 0.0050 \text{ kg/s}$ are $31.2 \mu\text{m}$, $62.6 \mu\text{m}$, $79.5 \mu\text{m}$, $101.6 \mu\text{m}$, and $139.7 \mu\text{m}$, respectively.

5.2.3. Effect of inlet pressure

The third set of tests was designed to get the impact of the inlet pressure p_{in} . The comparisons of water vapor mole fraction, droplet trajectory, and liquid film thickness of different inlet pressure were illustrated in Fig. 22, Fig. 23, and Fig. 24, respectively. According to the data in the figures, in the pressure test, a larger inlet pressure corresponds to a smaller range of evaporation and better droplet removal performance. When $p_{\text{in}} = 2.5 \text{ atm}$ and 2.0 atm , shock waves appear at the drain outlet, making part of the droplets enter the diffuser. The evaporation of liquid droplets increases the mole fraction of water vapor at the gas outlet. Furthermore, when $p_{\text{in}} = 2.0 \text{ atm}$, a large number of droplets fail to separate, resulting in a higher mole fraction of water vapor at the gas outlet than at the inlet. Meanwhile, the film thickness increases with the increase of inlet pressure. At $p_{\text{in}} = 3.0 \text{ atm}$, $p_{\text{in}} = 3.5 \text{ atm}$, and $p_{\text{in}} = 4.0 \text{ atm}$, there is little difference in the film thickness of the liquid outlet. Due to the shock wave at the drain outlet, the droplet thickness on the liquid outlet of $p_{\text{in}} = 2.0 \text{ atm}$ and $p_{\text{in}} = 2.5 \text{ atm}$ decreases.

5.3. Optimization analysis of separation efficiency

The three sets of tests in section 5.2 show the influences of inlet droplet diameter, inlet droplet mass flow rate, and inlet pressure on the droplet and liquid film behaviors in the supersonic separator. The results show that the inlet droplet mass flow rate determines the maximum liquid film thickness. The combined action of the three inlet conditions determines the droplet removal efficiency and water vapor removal efficiency. Therefore, this section will analyze and optimize the separation efficiency of the supersonic separator from the perspective of changing inlet parameters.

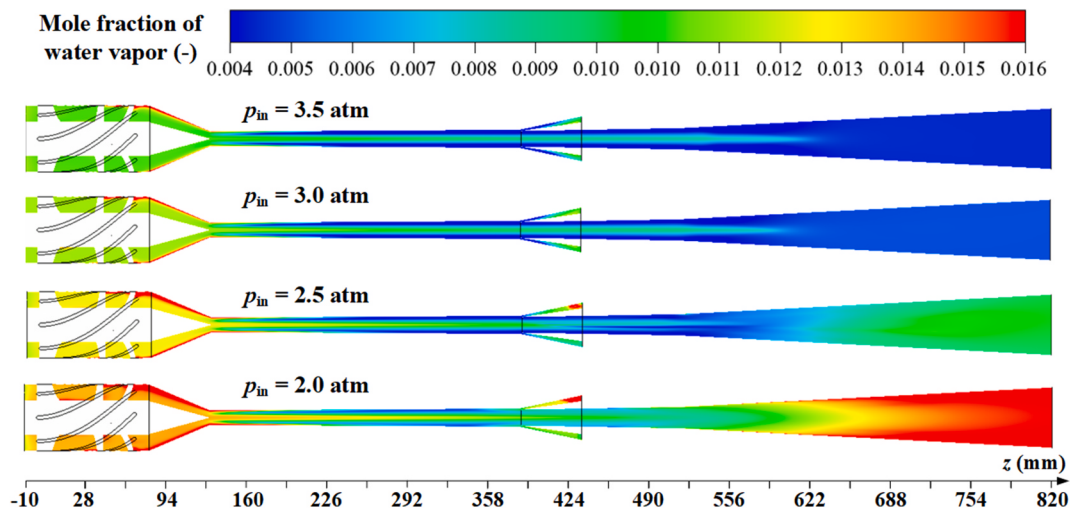


Fig. 22. Mole fraction of water vapor of the third group when $d_{p, in} = 2.2 \mu\text{m}$ and $q_{p, in} = 0.0015 \text{ kg/s}$.

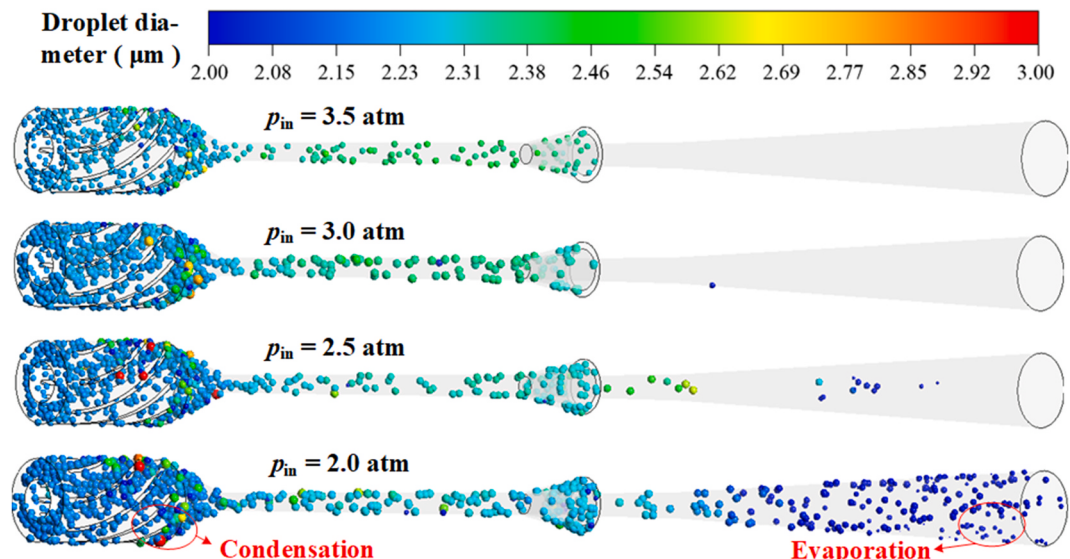


Fig. 23. Droplet trajectory of the third group when $d_{p, in} = 2.2 \mu\text{m}$ and $q_{p, in} = 0.0015 \text{ kg/s}$.

[Fig. 25](#) illustrates the effect of different inlet droplet diameters on the separation efficiency of the supersonic separator when other conditions are constant. With the increase of $d_{p, in}$, the droplet removal rate becomes higher, and when $d_{p, in} = 2.2 \mu\text{m}$, the droplet removal rate η_d reaches 100%. Then the vapor removal rate and dew point depression are used to evaluate the separation efficiency, the greater the value, the better the performance. Therefore, it is considered that the inlet droplet diameter of $2.2 \mu\text{m}$ with $\eta_v = 57.4\%$ and $\Delta T_d = 27.9 \text{ K}$ can produce the best separation efficiency.

[Fig. 26](#) effectively illustrates the separation efficiency at different inlet mass flow rates. It can be intuitively seen that the inlet mass flow rate of 0.0015 kg/s can better remove droplets and water vapor to improve the supersonic separator's separation efficiency. As for the effect of inlet pressure on separation efficiency, the general pattern can be seen in [Fig. 27](#). The higher the inlet pressure is, the better the separation efficiency will be. However, when the inlet pressure reaches a certain degree (above 3 atm), the influence of pressure change on the performance will become moderate. In summary, if $d_{p, in}$, $q_{p, in}$, and p_{in} are selected as $2.2 \mu\text{m}$, 0.0015 kg/s , and 3 atm (other conditions are certain), better separation efficiency can be obtained with $\eta_d = 100\%$, $\eta_v = 57.4\%$, and $\Delta T_d = 29.1 \text{ K}$.

6. Conclusion

A CFD model for three-field two-phase mass-heat transfer flow in a supersonic separator was established. The Eulerian-Lagrangian model simulates the gas and discrete droplets, and the Eulerian wall film model describes the liquid film behavior. The phase changes among the gas, droplets, and liquid film were considered. Formation, evaporation, separation, and stripping of the liquid film were considered non-negligible factors. The model was proved to have the ability to describe the gas-liquid separation process of the supersonic separator after being validated with three experiments. Then, using the proposed model, the three fields' behaviors and three-field heat and mass transfer interactions in the supersonic separator were excavated. The influence of different inlet conditions on condensation and separation was discovered, and the effect of heterogeneous growth on separation efficiency was also discussed. Furthermore, the optimal separation efficiency analysis was carried out on this basis. The main conclusions are as follows:

- (1) Four stages of the liquid film in supersonic separation are proposed: the formation stage due to droplet deposition, the

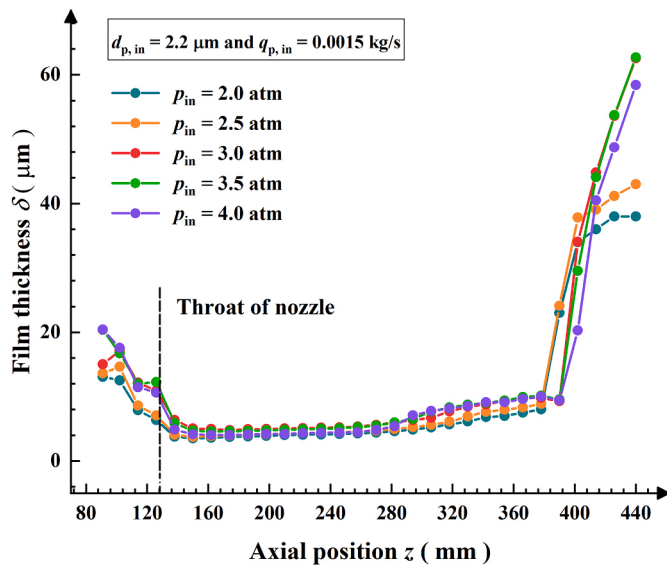


Fig. 24. Film thickness distributions of the third group when $d_{p,in} = 2.2 \mu\text{m}$ and $q_{p,in} = 0.0015 \text{ kg/s}$.

acceleration stage due to phase change of the liquid film under high shear force, the development stage because of a stronger deposition than entrainment, and the deceleration stage after the gas and film are separated, respectively.

- (2) Under the typical condition, when a low-temperature environment is generated, condensation is dominant to gas-liquid interaction in the supersonic separator, at which time the water vapor mole fraction reduces to 0.0050 at the minimum. The phase change rate of gas-film mass transfer varies from $-2 \times 10^{-3} \text{ kg s}^{-1} \text{ m}^{-2}$ and $8 \times 10^{-3} \text{ kg s}^{-1} \text{ m}^{-2}$. The droplet-film interaction has a great influence on the formation and development of the liquid film.
- (3) $q_{p,in}$ determines the maximum film thickness at the liquid outlet, while $d_{p,in}$ and p_{in} codetermines the minimum film thickness. When $q_{p,in} = 0.001 \text{ kg/s}$, the maximum film thickness is about 85.2 μm .
- (4) If $d_{p,in}$ is too large, the droplets will hit the wall and collect in the nozzle convergent section. The condensation core will be lost in advance, and the water vapor removal rate will be affected. If $d_{p,in}$ is too small or $q_{p,in}$ is too large, a large number of droplets will enter the gas diffuser, and the removal rate of droplets and water vapor will be poor. When $p_{in} \geq 3 \text{ atm}$, all droplets are removed, and the influence of p_{in} on separation efficiency becomes weak.
- (5) The influence of droplet heterogeneous growth on the flow field in a supersonic separator is significant. Proper droplet size and mass flow rate can effectively promote the condensation of water

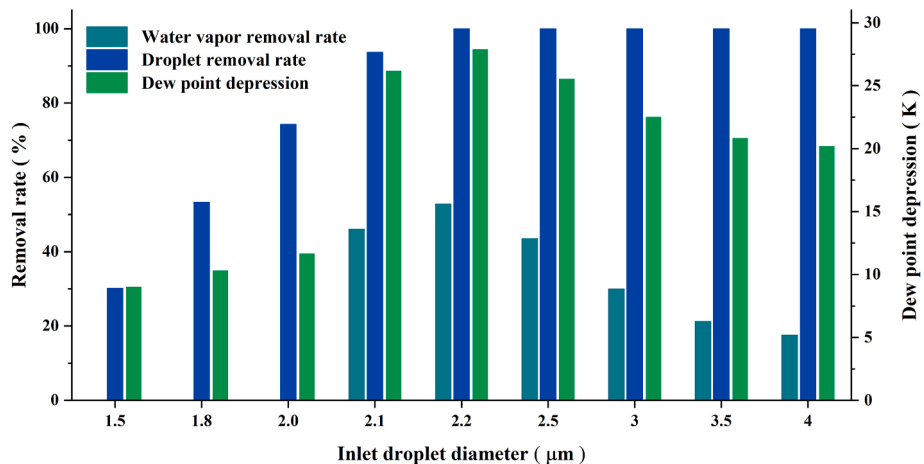


Fig. 25. The separation efficiency of the supersonic separator with different inlet droplet diameters when $q_{p,in} = 0.001 \text{ kg/s}$ and $P_{in} = 3 \text{ atm}$.

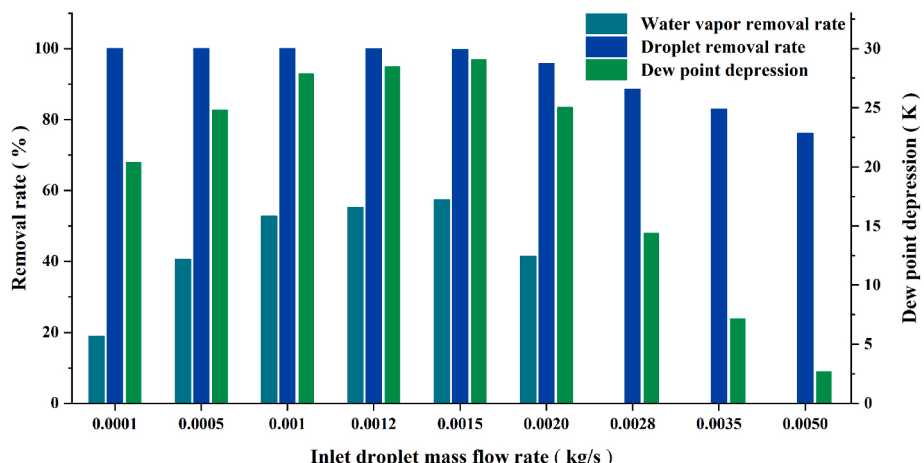


Fig. 26. The separation efficiency of the supersonic separator with different inlet droplet mass flow rates when $d_{p,in} = 2.2 \mu\text{m}$ and $P_{in} = 3 \text{ atm}$.

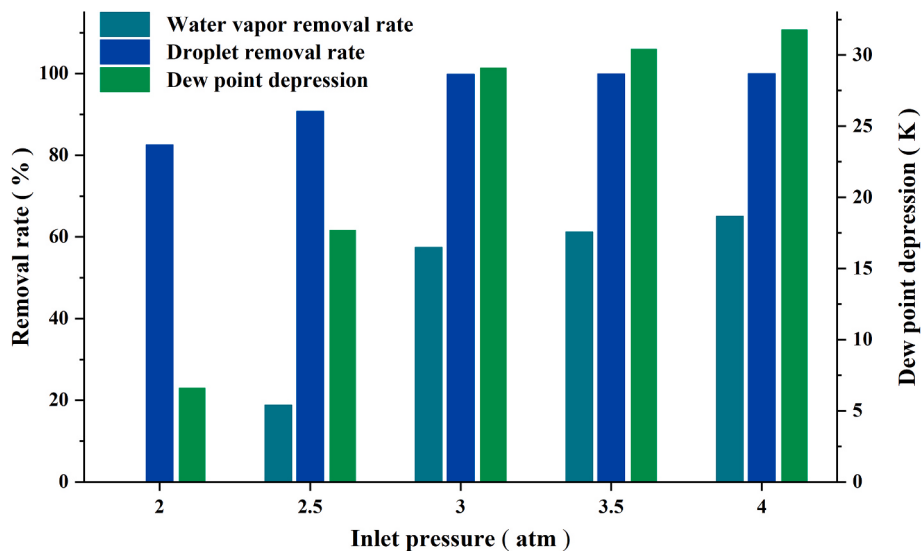


Fig. 27. The separation efficiency of the supersonic separator with different inlet pressures when $d_{p,in} = 2.2 \mu\text{m}$ and $q_{p,in} = 0.0015 \text{ kg/s}$.

vapor and improve separation efficiency. If $d_{p,in}$, $q_{p,in}$, and p_{in} are selected as $2.2 \mu\text{m}$, 0.0015 kg/s , and 3 atm , the better separation efficiency can be obtained with $\eta_d = 100\%$, $\eta_v = 57.4\%$, and $\Delta T_d = 29.1 \text{ K}$.

Data Availability Statement: The research data supporting this publication are provided within this paper.

Author statement

Hongbing Ding: Conceptualization, Supervision, Roles/Writing – original draft, Yu Zhang: Formal analysis, Investigation, Writing – review & editing, Chunqian Sun: Formal analysis, Investigation, Yan Yang: Methodology, Discussion, Reviewing, Chuang Wen: Supervision, Visualization, Methodology, Validation.

Declaration of competing interest

The authors declare that they have no known competing financial interests or personal relationships that could have appeared to influence the work reported in this paper.

Data availability

No data was used for the research described in the article.

Acknowledgment

This work is supported in part by National Natural Science Foundation of China under Grant 51876143, 61873184, and 61627803.

References

- [1] Shooshtari SHR, Shahsavand A. Maximization of energy recovery inside supersonic separator in the presence of condensation and normal shock wave. Energy 2017; 120:153–63.
- [2] Park J, Yoon S, Oh S, Kim Y, Kim J. Improving energy efficiency for a low-temperature CO₂ separation process in natural gas processing. Energy 2021;214: 118844.
- [3] Michaelides EE. Thermodynamic analysis and power requirements of CO₂ capture, transportation, and storage in the ocean. Energy 2021;230:120804.
- [4] Szoplik J. Improving the natural gas transporting based on the steady state simulation results. Energy 2016;109:105–16.
- [5] Xu G, Xu C, Wang M, Cai J, Chen Z, Li X. Influence of nickel foam on kinetics and separation efficiency of hydrate-based Carbon dioxide separation. Energy 2021; 231:120826.
- [6] Bian J, Cao X, Yang W, Edem MA, Yin P, Jiang W. Supersonic liquefaction properties of natural gas in the Laval nozzle. Energy 2018;159:706–15.
- [7] Bian J, Cao X, Yang W, Song X, Xiang C, Gao S. Condensation characteristics of natural gas in the supersonic liquefaction process. Energy 2018;168:99–110.
- [8] Secchi R, Innocenti G, Fiaschi D. Supersonic Swirling Separator for natural gas heavy fractions extraction: 1D model with real gas EOS for preliminary design. J Nat Gas Sci Eng 2016;34:197–215.
- [9] Park C, Kim C, Lee S, Lim G, Lee S, Choi Y. Effect of control strategy on performance and emissions of natural gas engine for cogeneration system. Energy 2015;82:353–60.
- [10] Karimi A, Abdi MA. Selective dehydration of high-pressure natural gas using supersonic nozzles. Chem Eng Process: Process Intensif 2009;48:560–8.
- [11] Fan Y, Zhang C, Jiang L, Zhang X, Qiu L. Exploration on two-stage latent thermal energy storage for heat recovery in cryogenic air separation purification system. Energy 2022;239:122111.
- [12] Brigagão GV, Arinelli LDO, de Medeiros JL, Araújo ODQF. Low-pressure supersonic separator with finishing adsorption: higher exergy efficiency in air pre-purification for cryogenic fractionation. Separ Purif Technol 2020;248:116969.
- [13] Cao X, Guo D, Sun W, Zhang P, Ding G, Bian J. Supersonic separation technology for carbon dioxide and hydrogen sulfide removal from natural gas. J Clean Prod 2021;288.
- [14] Wang Y. Analysis for spiral vortex and effect of profile of nozzle and swirler on performance of supersonic separator. Chem. Eng. Proc. - Proc. Intensif. 2020;147.
- [15] Sun W, Cao X, Yang W, Jin X. Numerical simulation of CO₂ condensation process from CH₄-CO₂ binary gas mixture in supersonic nozzles. Separ Purif Technol 2017; 188:238–49.
- [16] Zheng H, Su Y, Zheng L, Ke H. Numerical simulation of CO₂ and dye separation for supercritical fluid in separator. Separ Purif Technol 2020;236:116246.
- [17] Teixeira AM, Arinelli LDO, de Medeiros JL, Araújo ODQF. Economic leverage affords post-combustion capture of 43% of carbon emissions: supersonic separators for methanol hydrate inhibitor recovery from raw natural gas and CO₂ drying. J Environ Manag 2019;236:534–50.
- [18] Yudakov A, Vlasenko V, Slesarenko V. Comparative study of the combined supersonic separator and vortex tube performance for hydrocarbon gas drying. Chem Eng Technol 2021;44:773–81.
- [19] Arinelli LDO, de Medeiros JL, de Melo DC, Teixeira AM, Brigagão GV, Passarelli FM, et al. Carbon capture and high-capacity supercritical fluid processing with supersonic separator: natural gas with ultra-high CO₂ content. J Nat Gas Sci Eng 2019;66:265–83.
- [20] Brigagão GV, Arinelli LDO, de Medeiros JL, Araújo ODQF. A new concept of air pre-purification unit for cryogenic separation: low-pressure supersonic separator coupled to finishing adsorption. Separ Purif Technol 2019;215:173–89.
- [21] Ma C, Wang Y, Yu Y, Ren W, Hu D. Structure improvements and performance study of Supersonic Separation device with reflux channel. Chem. Eng. Proc.- Proc. Intensif. 2019;138:73–85.
- [22] Li Z, Manh TD, Gerdroobary MB, Nam ND, Moradi R, Babazadeh H. The effect of sinusoidal wall on hydrogen jet mixing rate considering supersonic flow. Energy 2020;193:116801.
- [23] Zhang H, Liu Q. Numerical investigation on performance of moisture separator: experimental validation, applications and new findings. Ann Nucl Energy 2020; 142.
- [24] Chen B, Wang B, Mao F, Wen J, Tian R, Lu C. Experimental study of droplet impacting on inclined wetted wall in corrugated plate separator. Ann Nucl Energy 2020;137.
- [25] Medeiros. Offshore processing of CO₂-rich natural gas with supersonic separator.

- [26] Wen C, Li A, Walther JH, Yang Y. Effect of swirling device on flow behavior in a supersonic separator for natural gas dehydration. *Separ Purif Technol* 2016;168:68–73.
- [27] Interlenghi SF, de Medeiros JL, Araujo ODQF. On small-scale liquefaction of natural gas with supersonic separator: energy and second law analyses. *Energy Convers Manag* 2020;221.
- [28] Arinelli LDO, Trotta TAF, Teixeira AM, de Medeiros JL, Araújo ODQF. Offshore processing of CO₂ rich natural gas with supersonic separator versus conventional routes. *J Nat Gas Sci Eng* 2017;46:199–221.
- [29] Bian J, Cao X, Yang W, Guo D, Xiang C. Prediction of supersonic condensation process of methane gas considering real gas effects. *Appl Therm Eng* 2020;164.
- [30] Li H, Anglart H. Prediction of dryout and post-dryout heat transfer using a two-phase CFD model. *Int J Heat Mass Tran* 2016;99:839–50.
- [31] Ding H, Sun C, Wang C, Wen C, Tian Y. Prediction of dehydration performance of supersonic separator based on a multi-fluid model with heterogeneous condensation. *Appl Therm Eng* 2020;171.
- [32] Liu Y, Cui J, Li WZ. A two-phase, two-component model for vertical upward gas–liquid annular flow. *Int J Heat Fluid Flow* 2011;32:796–804.
- [33] Adechy D, Issa RL. Modelling of annular flow through pipes and T-junctions. *Comput Fluids* 2004;33:289–313.
- [34] Yang Y, Wen C. CFD modeling of particle behavior in supersonic flows with strong swirls for gas separation. *Separ Purif Technol* 2017;174:22–8.
- [35] Wen C, Cao X, Yang Y, Zhang J. Evaluation of natural gas dehydration in supersonic swirling separators applying the Discrete Particle Method. *Adv Powder Technol* 2012;23:228–33.
- [36] Liu Liu, Li. Investigation on separation efficiency in supersonic separator with gas-droplet flow based on DPM approach. *Separ Sci Technol* 2014;49.
- [37] Chen J, Jiang W, Lai X, Cao X, Bian J, Bi Z. Study on the influence of wall-mounted cyclone on the purification and separation performance of supersonic separator. *Chem. Eng. Proc.- Proc. Intensif.* 2020;150:107898.
- [38] Wang Y, Yu Y, Hu D, Xu D, Yi L, Zhang Y, et al. Improvement of drainage structure and numerical investigation of droplets trajectories and separation efficiency for supersonic separators. *Chem. Eng. Proc.- Proc. Intensif.* 2020;151.
- [39] Haghghi M, Hawboldt KA, Abedinzadeh Abdi M. Supersonic gas separators: review of latest developments. *J Nat Gas Sci Eng* 2015;27:109–21.
- [40] Ding H, Sun C, Wen C, Liang Z. The droplets and film behaviors in supersonic separator by using three-field two-fluid model with heterogenous condensation. *Int J Heat Mass Tran* 2021;122315.
- [41] Niknam PH, Mortaheb HR, Mokhtarani B. Dehydration of low-pressure gas using supersonic separation: experimental investigation and CFD analysis. *J Nat Gas Sci Eng* 2018;52:202–14.
- [42] Vyazov YN, Prikhodko VG, Yarygin IV. Mach number effect on droplet phase angular distribution behind a nozzle under near-wall liquid film outflow with co-current gas flow into vacuum. *J Phys Conf* 2021;1867.
- [43] Pouriyeh HN, Daniell F, Hamid RM, Babak M. Numerical investigation of multiphase flow in supersonic separator considering inner body effect. *Asia Pac J Chem Eng* 2019;14.
- [44] Wang P, Jiang J, Li S, Yang X, Luo X, Wang Y, et al. Numerical investigation on the fluid droplet separation performance of corrugated plate gas–liquid separators. *Separ Purif Technol* 2020;248:117027.
- [45] Han J, Feng J, Hou T, Chen W, Peng X. Numerical and experimental study on gas–water separators for a PEMFC system. *Int J Green Energy* 2021;18.
- [46] Shunyang L, Pengfei W, Xiangyu L, Yucheng W, Xuelong Y, Amrit KT, et al. Numerical analysis of chevron demisters with drainage hooks in optimizing separation performance. *Int J Heat Mass Tran* 2020;152.
- [47] Yuan S, Fan Y, Chen B, Li J, Gao L, Zhang S. Forming and stripping of the wall film and the influence on gas–liquid separation. *Asia Pac J Chem Eng* 2020;15:e2447.
- [48] Deng Y, Zhang L, Hou H, Yu B, Sun D. Modeling and simulation of the gas–liquid separation process in an axial flow cyclone based on the Eulerian–Lagrangian approach and surface film model. *Powder Technol* 2019;353:473–88.
- [49] Zhou H, Jin Y, Zhu L, Li Z. Numerical simulation of droplets re-entrainment in baffle demister. *Part Sci Technol* 2021;40:567–75.
- [50] M In P Ak. Numerical simulation of a supersonic separator. *J Phys Conf* 2019;1399.
- [51] Interlenghi SF, Silva RDPF, de Medeiros JL, Araújo ODQF. Low-emission offshore Gas-To-Wire from natural gas with carbon dioxide: supersonic separator conditioning and post-combustion decarbonation. *Energy Convers Manag* 2019;195:1334–49.
- [52] Alnoush W, Castier M. Shortcut modeling of natural gas supersonic separation. *J Nat Gas Sci Eng* 2019;65:284–300.
- [53] Wen C, Cao X, Yang Y, Zhang J. Swirling effects on the performance of supersonic separators for natural gas separation. *Chem Eng Technol* 2011;34.
- [54] Ma Q, Hu D, He G, Hu S, Liu W, Xu Q, et al. Performance of inner-core supersonic gas separation device with droplet enlargement method. *Chin J Chem Eng* 2009;17:925–33.
- [55] Oberkampf WL, Trucano TG. Verification and validation in computational fluid dynamics. *Prog Aero Sci* 2002;38:209–72.
- [56] Zhong X. An improved generalized watson equation for prediction of latent heat of vaporization. *Chem Eng Commun* 2010;29.
- [57] O'Rourke P. Collective drop effects on vaporizing liquid sprays. Princeton University; 1981.
- [58] Ounis H, Ahmadi G, McLaughlin JB. Brownian diffusion of submicrometer particles in the viscous sublayer. *J Colloid Interface Sci* 1991;143.
- [59] Wood A. Textbook of sound. G. Bell and Sons Ltd.; 1944.
- [60] de Medeiros JL, Arinelli LDO, Araújo ODQF. Speed of sound of multiphase and multi-reactive equilibrium streams: a numerical approach for natural gas applications. *J Nat Gas Sci Eng* 2017;46:222–41.
- [61] Reznickova J, Petrychkovych R, Vejrazka J, Setnickova K, Uchytil P. Gas separation ability of the liquid bubble film. *Separ Purif Technol* 2016;166:26–33.
- [62] Frank T. Parallele Algorithmen für die numerische Simulation dreidimensionaler, disperter Mehrphasenströmungen und deren Anwendung in der Verfahrenstechnik. Chemnitz, Techn. Univ., Habil-Schr. Shaker Verlag; 2002.
- [63] Moore D. Two-phase steam flow in turbines and separators. Hemisphere Publishing Co.; 1976.
- [64] Yang Y, Walther JH, Yan Y, Wen C. CFD modeling of condensation process of water vapor in supersonic flows. *Appl Therm Eng* 2017;115:1357–62.
- [65] Xianmao W, Huajian C, Michael C, Tenglong C, Jun W. Prediction of falling film evaporation on the AP1000 passive containment cooling system using ANSYS FLUENT code. *Ann Nucl Energy* 2016;95.
- [66] Wang X, Chang H, Corradini M, Cong T, Wang J. Prediction of falling film evaporation on the AP1000 passive containment cooling system using ANSYS FLUENT code. *Ann Nucl Energy* 2016;95:168–75.
- [67] Es T, Az T, S G. Polymer electrolyte fuel cell model. *J Electrochem Soc* 2019;138.
- [68] Jh A, Jd J, Eavd H. An experimental and numerical study of turbulent swirling flow in gas cyclones. *Chem Eng Sci* 1999;54.
- [69] Wang B, Xu DL, Chu KW, Yu AB. Numerical study of gas–solid flow in a cyclone separator. *Appl Math Model* 2006;30:1326–42.
- [70] Kashuai D, Po H, Zhen H, Iztok T. Numerical investigation of water film evaporation with the countercurrent air in the asymmetric heating rectangular channel for passive containment cooling system. *Sci Technol Nucl Ins* 2020;2020.